Prospects for measuring the time variation of astrophysical neutrino sources at dark matter detectors

Yi Zhuang,[1] Louis E. Strigari,[1] Lei Jin,[2] and Samiran Sinha[3]
[1]*Department of Physics and Astronomy, Mitchell Institute for Fundamental Physics and Astronomy,*
Texas A&M University, College Station, Texas 77843, USA
[2]*Department of Mathematics and Statistics, Texas A&M University-Corpus Christi,*
Corpus Christi, Texas 78412, USA
[3]*Department of Statistics, Texas A&M University, College Station, Texas 77843, USA*

(Received 29 February 2024; accepted 11 July 2024; published 26 August 2024)

We study the prospects for measuring the time variation of solar and atmospheric neutrino fluxes at future large-scale xenon and argon dark matter detectors. For solar neutrinos, a yearly time variation arises from the eccentricity of Earth's orbit and, for charged current interactions, from a smaller energy-dependent day-night variation due to flavor regeneration as neutrinos travel through Earth. For a 100-ton xenon detector running for ten years with a xenon-136 fraction of $\lesssim 0.1\%$, in the electron recoil channel a time-variation amplitude of about 0.8% is detectable with a power of 90% and the level of significance of 10%. This is sufficient to detect time variation due to eccentricity, which has amplitude of ~3%. In the nuclear recoil channel, the detectable amplitude is about 10% under current detector resolution and efficiency conditions, and this generally reduces to about 1% for improved detector resolution and efficiency, the latter of which is sufficient to detect time variation due to eccentricity. Our analysis assumes both known and unknown periods. We provide scalings to determine the sensitivity to an arbitrary time-varying amplitude as a function of detector parameters. Identifying the time variation of the neutrino fluxes will be important for distinguishing neutrinos from dark matter signals and other detector-related backgrounds and extracting properties of neutrinos that can be uniquely studied in dark matter experiments.

DOI: 10.1103/PhysRevD.110.043037

I. INTRODUCTION

Over the past several decades, direct dark matter detection experiments have made tremendous progress in constraining weak-scale particle dark matter [1,2]. Future larger-scale detectors will be sensitive to not only particle dark matter, but also astrophysical neutrinos and various other rare-event phenomenology [3]. The most prominent of the neutrino signals are from the Sun, the atmosphere, and the diffuse supernova neutrino background (DSNB) [4]. Understanding these signals has important implications for the future of particle dark matter searches, but also for understanding the nature of the sources and the properties of neutrinos [5].

Various methods have been proposed to distinguish neutrinos and a possible dark matter signal. These include exploiting the energy distribution of nuclear recoils between neutrinos and dark matter [6,7], considering spectrum of ionization of electrons from nuclear recoils [8], the differences in arrival directions [9], and the differences in the periodicities of the signal [10,11]. New physics in the neutrino sector may also change the nature of the predicted neutrino signal [12–14] and provide a method to discriminate from dark matter.

Here we examine the time variations of the neutrino signals in more detail and study the prospects for measuring these time variations. For solar neutrinos, the time variation of the flux is due to the eccentricity of Earth's orbit and the day-night effect. The former is independent of the neutrino flavor, while the latter, which results from neutrino interactions with the matter as they pass through Earth, is flavor dependent. Both effects are present in a dark matter experiment through the nuclear recoil and electron recoil channels. Beyond solar neutrinos, there may be detectable time variation of other components of the astrophysical neutrino flux. Because of the solar cycle, there is a time variation of the atmospheric neutrino flux which is ~10%–30% [15] depending on the detector location. We present the first estimates of the detectability of the time variation of the atmospheric neutrino flux given realistic future detector configurations.

Identifying the time variation for the different neutrino sources is important for properly extracting the signal and distinguishing it from dark matter [4,16]. In addition, it is important to characterize these signals to constrain neutrino properties. Previous studies of neutrinos in dark matter experiments have only considered the time variation of solar neutrinos as being due to the eccentricity of Earth's orbit and for idealized values of the nuclear recoil threshold [10]. In addition to examining more realistic and updated detector configurations, we consider the prospects for measuring time variation of solar neutrinos using the neutrino-electron elastic scattering channel for the first time.

Solar neutrino experiments have previously searched for time variations in their signals, including experiments that have successfully established time variation due to the eccentricity of Earth's orbit [17,18] and the day-night effect [19]. These experiments each used a range of statistical techniques to identify the time-variable signal. As part of our analysis, we rigorously compare the different statistical methodologies for extracting the time-varying signal. We present results for the sensitivity of given experiments to time-varying amplitudes and quantify the prospects for signal extraction as a function of experimental sensitivity and background levels.

This paper is organized as follows. In Sec. II, we briefly describe the signals and the models for the detector efficiency. In Sec. III we describe the periodic signals used in this work, and also we summarize the previous experiments that have searched for neutrino periodicity. Next, in Sec. IV, we review the statistical methodologies used in our analysis. In Sec. V, we describe the simulation strategy, compare statistical methods, and introduce the signal-to-noise ratio as a convenient estimation tool. Then, in Sec. VI, we present our resulting projections and, in Sec. VII, the discussion and conclusions.

II. EVENT RATES AT DIFFERENT DETECTORS

A. Theoretical calculation

Figures 1 and 2 show the electron and nuclear recoil spectra for the solar, atmospheric, and DSNB spectra for xenon and argon targets. The nuclear recoil spectrum uses the neutral current coherent elastic neutrino-nucleus

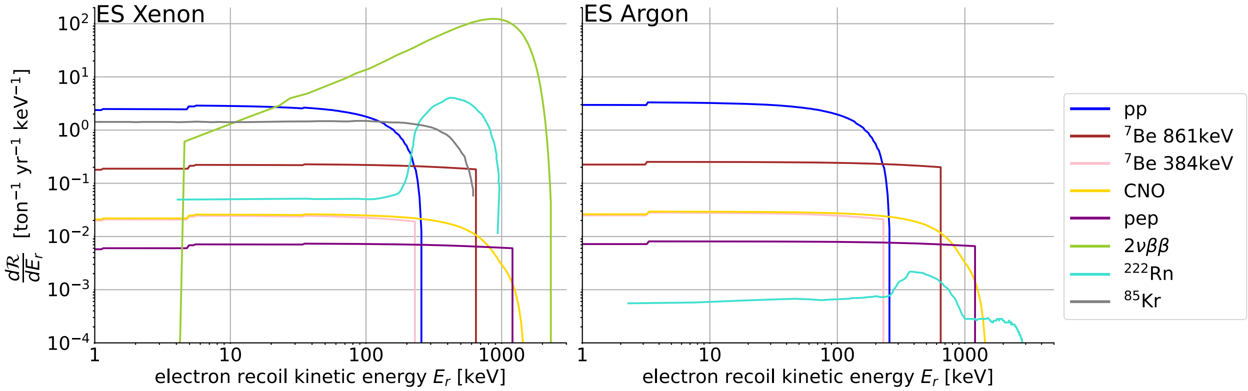

FIG. 1. Neutrino-electron ES spectra for xenon (left) and argon (right) for solar and experimental background components. For ES argon, we consider ^{222}Rn as the background [23].

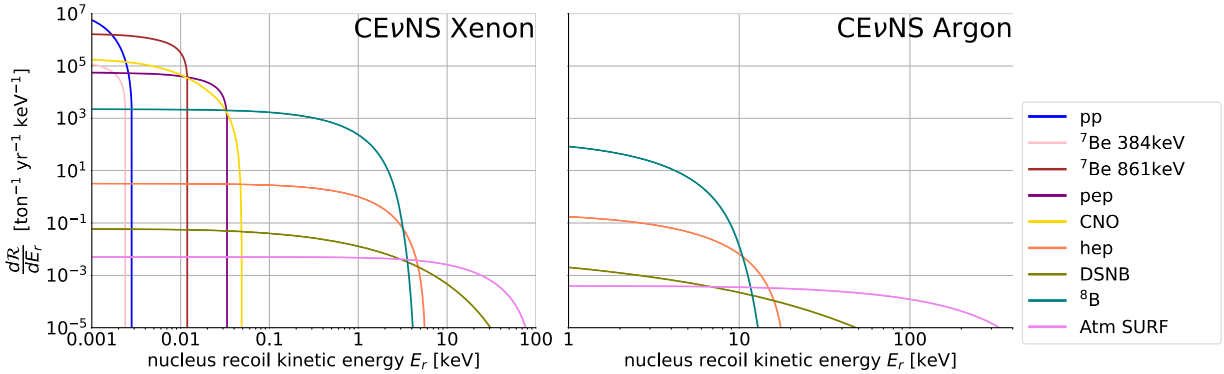

FIG. 2. CEνNS spectra for xenon (left) and argon (right). Shown are the components of the solar, atmospheric, and DSNB spectra. The atmospheric spectra are shown for the SURF detector location.

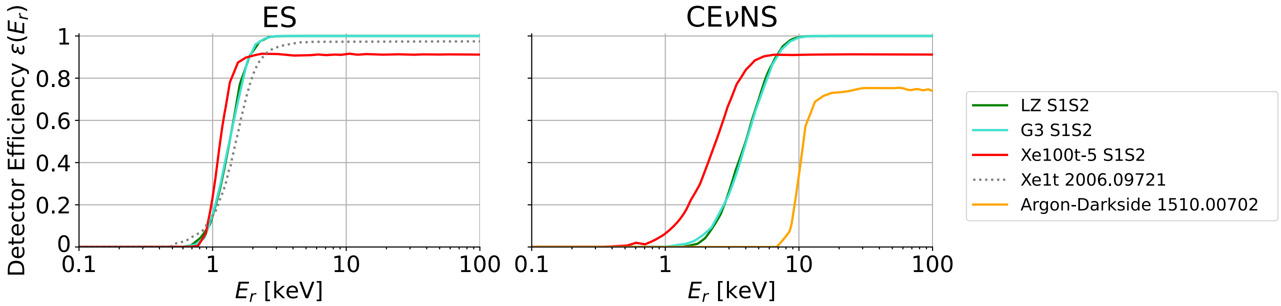

FIG. 3. Different detector efficiency models from NEST simulations (LZ, G3, Xe100t-5) and current experiments (Argon-Darkside, Xe1T). Left: solid curves are LZ, G3, and Xe100t-5 for xenon ES. The dotted curve is the efficiency from Xenon1T [27]. Right: solid curves are LZ, G3, and Xe100t-5 for the xenon nuclear recoil CEνNS channel. The orange solid curve is the efficiency from Darkside-50 [28] for nuclear recoils in argon.

scattering (CEνNS) channel, and the electron recoil channel uses charged current neutrino-electron elastic scattering (ES). We refer to previous literature for details of these calculations [20]. Here we simply highlight the components of the spectrum as a function of recoil energy to get a sense of the recoil threshold required to detect each component. For solar neutrinos, we used the high metallicity model for the normalization [21]. We also show the appropriate experimental background components [22].

In addition to the energy dependence shown in Figs. 1 and 2, for several of the neutrino components there is a time variation to the flux. For solar neutrinos, since the time variation due to the eccentricity of Earth's orbit affects all flavors, it will be present in both the CEνNS and the ES channels. For charged current detection channels, the day-night effect due to oscillations is present in the ES channel. For atmospheric neutrinos, the time variation from the solar modulation of the atmospheric neutrino flux [15] affects all flavors and is detectable through CEνNS. Of the spectra shown in Fig. 2, the only essentially steady-state component is the DSNB, which has a cosmological origin [24]. In the section below, we describe our parameterization of each of these time-varying components in more detail.

B. Adding resolution and detector efficiency

To estimate the detector efficiency and resolution in xenon, we use the noble element simulation technique (NEST) [25] code. Neutrinos (or dark matter particles) interact with the gas in the detector, producing a scintillation signal, S1, and ionization electrons, which then drift along the electric field to produce a scintillation signal, S2. The NEST code simulates the detection of events in the space of S1 and S2. For the NEST configurations, we compare several possible options. Similar to previous studies, we consider the all enhanced parameters "Xe100t-5"[1] [26]. We also use the specific experimental files LZ[2] and G3.[3] For all cases, we do not select a specific region of interest (ROI), so the signal encompass all available space for electron and nuclear recoils.

With this setup, we estimate the detector efficiency as a function of the true nuclear or electron recoil energy. To obtain the efficiency, we simulate 10^7 random recoil energies uniformly over the range $[0-100]$ keV within the detector. After processing through NEST, each simulated energy corresponds to a specific S1 and S2. We bin the detected events in recoil energy space, count the number of events with both valid S1/S2 [27], and divide the valid counts by the total number of events in each energy bin.

The results for the ES and CEνES efficiencies are shown in Fig. 3. For comparison, we show the ES efficiency used by Xenon1T [27], which is similar to our Xe100t-5, LZ, and G3 curves, with the differences between them likely explained by using different detector parameters, including the ROI and the recoil energies simulated. For xenon, the electron recoil efficiency drops to zero rapidly below $\sim$1 keV and is nearly 100% above this energy.

To obtain the event rate modified by resolution and detector efficiencies, we integrate from a threshold energy E_{thrd} to an end point energy E_{end} and obtain $\mathcal{R} = \int_{E_{\mathrm{thrd}}}^{E_{\mathrm{end}}} (d\mathcal{R}/dE_r) dE_r$, where

$$\frac{d\mathcal{R}}{dE_r} = \epsilon(E_r) \int dE_r' \frac{d\mathcal{R}(E_r')}{dE_r'} \frac{1}{\sqrt{2\pi\sigma^2(E_r')}} e^{-\frac{1}{2}\frac{(E_r-E_r')^2}{\sigma^2(E_r')}},$$

where E_r' is the true recoil energy, E_r is the detected recoil energy, $\sigma(E_r')$ is the resolution at the true recoil energy, and $\epsilon(E_r)$ is the detector efficiency at the detected recoil energy.

Different resolution and efficiency models for different nuclear targets that we use for our analysis are summarized in Tables I and II. For xenon our resolution and efficiency

---

[1] https://zenodo.org/records/3653516“Detector_Xe100t_5.hh.

[2] https://github.com/NESTCollaboration/nest/blob/master/include/Detectors/LZ_SR1.hh.

[3] https://github.com/NESTCollaboration/nest/blob/master/include/Detectors/Detector_G3.hh.

TABLE I. Target, resolution model, detector efficiency model, recoil energy threshold, recoil energy end point, components experiencing time variation, and components that have constant rate constant in time in the ES channel. $f_{2\nu\beta\beta}$ is the fraction of the remaining $2\nu\beta\beta$ background after depletion of ^{136}Xe.

Channel	Target	Resolution model $\sigma(E_r)$	Efficiency model $\epsilon(E_r)$	E_{thrd} (keV)	E_{end} (keV)	Signal components ($\mathrm{ton}^{-1}\ \mathrm{yr}^{-1}$)	Background components ($\mathrm{ton}^{-1}\ \mathrm{yr}^{-1}$)
ES	Xe	Ideal	Ideal	1	650	pp, ^{7}Be 861, ^{7}Be 384, pep, CNO	$f_{2\nu\beta\beta} \times 2\nu\beta\beta$, ^{85}Kr, ^{222}Rn
		$\left(0.31\sqrt{\frac{E_r}{\mathrm{keV}}} + 0.0035\frac{E_r}{\mathrm{keV}}\right)$ keV [27]	Xe100t-5	0	790		
	Ar	Ideal	Ideal	1	3400		^{222}Rn
		$0.1E_r$	Not applicable	100	3400		

TABLE II. Same as Table I except for the CEνNS channel.

Channel	Target	Resolution model $\sigma(E_r)$	Efficiency model $\epsilon(E_r)$	E_{thrd} (keV)	E_{end} (keV)	Signal components ($\mathrm{ton}^{-1}\ \mathrm{yr}^{-1}$)	Background components ($\mathrm{ton}^{-1}\ \mathrm{yr}^{-1}$)
CEνNS	Xe	Ideal	Ideal	1	4	^{8}B	Not applicable
		$\left(0.31\sqrt{\frac{E_r}{\mathrm{keV}}} + 0.0035\frac{E_r}{\mathrm{keV}}\right)$ keV [27]	Xe100t-5	0	9		
			LZ				
			G3				
	Ar	Ideal	Ideal	1	13		
		$0.1E_r$	Darkside	0	29		

models rely on NEST simulations as described above. For our argon ES resolution and efficiency model, we choose $E_{\mathrm{thrd}} = 100$ keV in order to determine how our results are affected by choosing a threshold characteristic of current experiments.

III. PHYSICAL PERIODIC SIGNALS OF INTEREST

A. Solar yearly modulation

The slight eccentricity ϵ to Earth's orbit around the Sun induces a yearly variation in the neutrino flux. The time dependence of the flux is parameterized as [29]

$$\phi(t) = \frac{\mathcal{R}_\odot}{4\pi r^2(t)} \approx \frac{\mathcal{R}_\odot}{4\pi r_0^2}\left[1 + 2\epsilon\cos\left\{\frac{2\pi(t-t_0)}{P}\right\}\right], \qquad (1)$$

where P denotes the periodicity measured in years, $r(t)$ is the distance between Earth and the Sun at time t measured in years (i.e., $0 \leq t \leq 1$), $r_0 = 1$ A.U., and $\mathcal{R}_\odot$ is the neutrino production rate in the Sun per unit time. The second term, $2\epsilon\cos\{2\pi(t-t_0)/P\}$, in Eq. (1) is responsible for the small time variation. The amplitude of the flux variation is approximately 0.03342 and has been measured by several experiments, including recently by Borexino [17]. t_0 for the solar neutrino is approximately 3 days (peaked on January 4, [10]). For standard assumptions for the dark matter velocity distribution, this time variation is out of phase with the standard modulation signal predicted from dark matter t_0 for dark matter is approximately 152 days (peaked on June 2, [30]) and has been proposed as a means to separate neutrinos from dark matter signals [10].

B. Solar daily modulation

A second time variation in the solar neutrino flux is the day-night effect, which is due to the regeneration of the electron neutrino flux from matter effects as electron neutrinos pass through Earth. The day-night asymmetry is detectable for experiments sensitive to the electron neutrino flux through charged current interactions. Defining N_D and N_N as the number of day and night events, the day-night asymmetry A_{DN} is parametrized as [17]

$$A_{DN} = \frac{N_D - N_N}{0.5(N_D + N_N)} = \frac{2A_{d,DN}}{\sqrt{2}R_\odot},$$

where $A_{d,DN}$ is the amplitude of the daily modulation. Super-Kamiokande has now established the day-night effect for high energy ^{8}B neutrinos [19] with a measured amplitude of $\lesssim 3\%$ that is consistent with the LMA (large mixing angle)–MSW (Mikheyev-Smirnov-Wolfenstein) solution.

At lower energies, where solar neutrinos transitions are due to vacuum oscillations, the LMA-MSW solution predicts that the day-night modulation is much smaller, $\lesssim 0.1\%$. The best limits on the day-night modulation at these energies come from Borexino measurements of the

^{7}Be component [17]. Borexino is sensitive to electron recoils $\gtrsim 150$ keV, so is not sensitive to the modulation for the lower energy pp component. Since xenon- and argon-based dark matter experiments are sensitive to lower threshold, ~few keV electron recoils, they will extend limits on solar neutrino time variation and day-night effects to lower energies than have been previously studied. In our analysis, we simply compare the limits on daily modulation from dark matter detectors to the limits on the modulation obtained from Borexino.

C. Atmospheric neutrinos

We also study the prospects for identifying the time variation of the atmospheric neutrino flux. Atmospheric neutrinos are detected through the CEνNS channel, with a modulation amplitude that depends on the detector location. We model the atmospheric time variation with a sinusoidal function in a similar manner to Eq. (1). In this case, modulation of solar wind (solar cycle) has an 11-yr period. The solar wind affects the amount of cosmic rays entering the solar system, then entering Earth, where the primary cosmic ray (mostly proton) interacts with the atmosphere and produces atmospheric neutrinos and other secondary particles. So the atmospheric neutrino flux is also sensitive to the modulation with 11-yr period. And the amplitudes are given by the maximum difference between the solar minimum and maximum fluxes calculated in Ref. [15]. The flux differs for different detector locations because the geomagnetic field deflects the incoming cosmic ray and is location dependent, which we consider in our analysis below. For example, for the detector locations of China Jinping Underground Laboratory (CJPL), Kamioka, Laboratori Nazionali del Gran Sasso (LNGS), the Sanford Underground Research Facility (SURF), and SNOlab, the maximum amplitudes for time variation are $A_{atm} = [0.0459, 0.0382, 0.0461, 0.1475, 0.1327]$ [15], respectively, where A_{atm} and ω are defined through

$$\begin{aligned} \phi_{atm}(t) &= \bar{\phi}\{1 + A_{atm}\sin(\omega t)\}, \\ \bar{\phi} &= \frac{\phi_{09} + \phi_{14}}{2}, \\ A_{atm} &= \frac{\phi_{09} - \phi_{14}}{2\phi_{09}}, \\ \omega &= \frac{2\pi}{11\ \mathrm{yr}}. \end{aligned}$$

The quantities ϕ_{09} and ϕ_{14} are the fluxes in the years of 2009 and 2014, corresponding to solar minimum and solar maximum, respectively.

D. Previous experimental methods and results

Over the past several decades, multiple experiments have searched for possible periodic signals in neutrino data. To this point, the eccentricity has been measured by Borexino, and the day-night modulation due to charged current interactions has been established by Super-Kamiokande (SK). An upper limit of the diurnal modulation has been set by Borexino.

A typical data analysis procedure is to bin the observed data in time bins. Then, a Fourier transform is performed, a range of frequencies is scanned, and then peaks that correspond to possible periodic signals are found. The peaks are checked to determine if the power of the peak exceeds a certain threshold, such that the probability of the peak coming from noise (false-alarm probability) is low. The specific details of turning time-binned data into the periodogram, the error of the observed data, and the terminology describing the methods differ among the experimental analyses.

In Table III, we summarize the results from experiments at Homestake, Gran Sasso, Kamioka, Sudbury, Borexino, and IceCube. We refer to each paper for more details on their analysis methods. We characterize the experiments in terms of their run-time $\mathcal{T}$, assumed time binning Δt, frequency range scanned, the periodic signal of interests, and the results. These summarized results provide a point of comparison for our future projections for dark matter detectors.

IV. STATISTICAL METHODS FOR TIME-VARYING ANALYSIS

This section establishes our statistical methods for detecting solar and atmospheric neutrinos, specifically describing our methods for constructing the likelihood function. In this case, the null hypothesis H_0 is defined as a signal with a constant rate in time, while the alternative H_1 is defined as a signal whose rate of events varies in time with a period P and an amplitude A_d.

We use the following models under H_0 and H_1 to formulate our likelihood ratio test. Let n_i be the number of observed events in the time bin $(t_i, t_i + \Delta t)$. We assume that

$$n_i \equiv n(t_i) \sim \begin{cases} \mathrm{Pois}(\lambda\Delta t) & \text{under } H_0, \\ \mathrm{Pois}(\lambda_i) & \text{under } H_1, \end{cases}$$

where the expected number of events in the time bin $(t_i, t_i + \Delta t)$ under the assumption of H_1 is

$$\lambda_i \equiv \lambda(t_i) = \lambda \int_{t_i}^{t_i+\Delta t} \{1 + A\cos(\omega u) + B\sin(\omega u)\} du.$$

In the above formulation, λ, A, and B are unknown parameters, and ω is an unknown frequency. In λ_i, the background signal is $\lambda\Delta t$ and the time-varying signal is $\lambda \int_{t_i}^{t_i+\Delta t} \{A\cos(\omega u) + B\sin(\omega u)\} du$. Note that H_0 is a special case of H_1 as we obtain the null model by setting $A = B = 0$ in λ_i.

First, we assume that ω is known for a gentle exposition of the methodology. To test H_0 against H_1, we use the generalized likelihood ratio (GLR) method. The term

TABLE III. Summary of previous experimental results searching for time variation of solar neutrinos. The columns are (1) experiment, (2) signal of interest experiment searched for, (3) experimental exposure, (4) time binning used in the analysis, (5) scanned frequency range, (6) results of the analysis, along with specific comments where appropriate. Boxes are left blank in the experimental exposure and time binning columns for Homestake because that information was not provided. Boxes are left blank in the scanned frequency range column because in these cases the signal frequency is fixed at 1 yr and the amplitude (eccentricity) is obtained through the best fit.

Experiment	Signals of interest	$\mathcal{T}$	Δt	Scanned frequency range $(f_{\min}, f_{\max})$	Results
Homestake [31]	Quasibiennial periodicity $\frac{1}{2.2}$ yr^{-1}, Rieger periodicity $\frac{1}{157}$ day^{-1}			(0, 20) yr^{-1}	No evidence
	Solar rotation frequency			(12.4, 13.1) yr^{-1}	Peak at 12.88 yr^{-1} Significant at the 3% level
Gran Sasso [32]	Blind search	1594 days (Gallex) 1713 days (GNO) 3307 days (Gallex/GNO)	3 or 4 weeks	(0.04, 26) yr^{-1}	Peak at 6.37 yr^{-1} (Gallex/GNO) Peak at 2.9 yr^{-1} (GNO only)
	Eccentricity 1 yr^{-1}				Best-fit eccentricity $\epsilon = 0.0165$
Sudbury	Blind search	572.2 calendar days (D$_2$O) 762.7 calendar days (salt) [33,34]	1 day	($\frac{1}{10}$, 365.25) yr^{-1}	Peak at 0.296 day^{-1} (D$_2$O), 0.971 day^{-1} (salt), 0.417 day^{-1} (combined)
				($\frac{1}{10}$, 182.625) yr^{-1}	Peak at 0.408 day^{-1} (D$_2$O), 0.429 day^{-1} (salt), 0.413 day^{-1} (combined)
	7% amplitude 9.43 yr^{-1} Kamioka result			(9.33, 9.53) yr^{-1}	Best-fit amplitude 1.3% (combined)
	Eccentricity 1 yr^{-1}				Best-fit eccentricity $\epsilon = 0.0143$
Borexino	Diurnal modulation 1 day^{-1}	740.88 live days [35] phase I			Day-night asymmetry = 0.001
	Eccentricity 1 yr^{-1}	1456 astro days [36] phase II	30.43 days		Best-fit eccentricity $\epsilon = 0.0174$
			1 day 7 days		Peak at 1 yr^{-1}
	Eccentricity 1 yr^{-1}	~10 yr [17] phase II + III	30 days		Best-fit eccentricity $\epsilon = 0.0184$
	Carrington rotation 13.4 yr^{-1}, diurnal modulation 1 day^{-1}		8 hr	(1, 547) yr^{-1}	Day-night asymmetry = 0.003
Kamioka	Blind search	1871 elapsed days SK-1 [18,37–40]	10 days	(0.0002, 0.0987) day^{-1} [37]	Peak at 0.0726 day^{-1}
				(0, 50) yr^{-1} [18]	Peak at 9.42 yr^{-1}
				(0, 100) yr^{-1} [38]	Peak at 26.57 yr^{-1}
				(0, 40) yr^{-1} [38]	Alias peak at 9.42 yr^{-1}
			5 days	(0.0002, 0.19187) day^{-1} [37]	Peak at 0.1197 day^{-1} 0.0726 day^{-1} removed
				(0, 50) yr^{-1} [18,39]	Alias peak of 9.42 yr^{-1} at 26.52 yr^{-1} possible solar rotation
	Eccentricity 1 yr^{-1} [40]		1.5 months		Best-fit eccentricity $\epsilon = 0.021$
	Day-night difference [40]				Day-night asymmetry = $-0.021, -0.017$
	Blind search	5803 live days [41] SK-I, II, III, IV	5 days	(4e^{-4}, 0.2) day^{-1}	Peak at 0.126 day^{-1}
				(10^{-6}, 0.2) day^{-1}	Peak at 0.143 day^{-1}
	Eccentricity 1 yr^{-1}		$\frac{365.25}{12}$ days		Best-fit eccentricity $\epsilon = 0.0153$
IceCube [42]	Temperature-dependent variation of atmospheric neutrino flux	May 2012–May 2017	1 day 30 days		High statistics at 140 day^{-1} in the south region

generalized is used when at least one of H_0 and H_1 is a composite hypothesis; in our case, both are composite hypotheses. Reference [34] used the GLR method for identifying the periodicity of ^{8}B solar neutrino flux released by the SNO Collaboration. However, unlike [34], we obtain the expected number of events within a time bin by integrating the time-varying instantaneous rate function, which is an appropriate method, especially when the bin width is not very small. Moreover, besides applying to ^{8}B solar neutrinos, we use this model for all components of the solar and atmospheric neutrino flux. The GLR statistic is

$$\mathrm{GLR} = \frac{\max_\lambda \prod_{i=1}^{N_t} \frac{\lambda^{n_i} e^{-\lambda}}{n_i!}}{\max_{\lambda,A,B} \prod_{i=1}^{N_t} \frac{\lambda_i^{n_i} e^{-\lambda_i}}{n_i!}} = \frac{\max_\lambda \prod_{i=1}^{N_t} \lambda^{n_i} \exp(-\lambda)}{\max_{\lambda,A,B} \prod_{i=1}^{N_t} \lambda_i^{n_i} \exp(-\lambda_i)}. \tag{2}$$

The numerator of (2) is

$$(\hat{\lambda}_0 \Delta t)^{\sum_{i=1}^{N_t} n_i} \exp(-\hat{\lambda}_0 \Delta t N_t),$$

where $\hat{\lambda}_0 = \sum_{i=1}^{N_t} n_i / N_t \Delta t$ denotes the maximum likelihood estimator of λ under H_0. The denominator of (2) is

$$\prod_{i=1}^{N_t} \hat{\lambda}_i^{n_i} \exp(-\hat{\lambda}_i),$$

where $\hat{\lambda}_i = \hat{\lambda}_1 \int_{t_i}^{t_i+\Delta t} \{1 + \hat{A}\cos(\omega u) + \hat{B}\sin(\omega u)\} du$ with $\hat{\lambda}_1$, $\hat{A}$ and $\hat{B}$ being the solution of the following gradient equations (obtained by differentiating the log-likelihood function under H_1):

$$0 = \sum_{i=1}^{N_t} \left[\frac{n_i}{\lambda} - \int_{t_i}^{t_i+\Delta t} \{1 + A\cos(\omega u) + B\sin(\omega u)\} du \right], \tag{3}$$

$$0 = \sum_{i=1}^{N_t} \left\{ \frac{n_i \int_{t_i}^{t_i+\Delta t} \cos(\omega u) du}{\int_{t_i}^{t_i+\Delta t} \{1 + A\cos(\omega t_i) + B\sin(\omega u)\} du} - \lambda \int_{t_i}^{t_i+\Delta t} \cos(\omega u) du \right\}, \tag{4}$$

$$0 = \sum_{i=1}^{N_t} \left\{ \frac{n_i \int_{t_i}^{t_i+\Delta t} \sin(\omega u) du}{\int_{t_i}^{t_i+\Delta t} \{1 + A\cos(\omega t_i) + B\sin(\omega u)\} du} - \lambda \int_{t_i}^{t_i+\Delta t} \sin(\omega u) du \right\}. \tag{5}$$

Equation (3) yields

$$\lambda = \frac{\sum_{j=1}^{N_t} n_j}{\sum_{j=1}^{N_t} \int_{t_j}^{t_j+\Delta t} \{1 + A\cos(\omega u) + B\sin(\omega u)\} du},$$

and using this expression in (4) and (5) we obtain

$$\begin{aligned} 0 &= \sum_{i=1}^{N_t} \left[\frac{n_i}{\int_{t_i}^{t_i+\Delta t} \{1 + A\cos(\omega u) + B\sin(\omega u)\} du} - \frac{\sum_{j=1}^{N_t} n_j}{\sum_{j=1}^{N_t} \int_{t_j}^{t_j+\Delta t} \{1 + A\cos(\omega u) + B\sin(\omega u)\} du} \right] \int_{t_i}^{t_i+\Delta t} \cos(\omega v) dv, \\ 0 &= \sum_{i=1}^{N_t} \left[\frac{n_i}{\int_{t_i}^{t_i+\Delta t} \{1 + A\cos(\omega u) + B\sin(\omega u)\} du} - \frac{\sum_{j=1}^{N_t} n_j}{\sum_{j=1}^{N_t} \int_{t_j}^{t_j+\Delta t} \{1 + A\cos(\omega u) + B\sin(\omega u)\} du} \right] \int_{t_i}^{t_i+\Delta t} \sin(\omega v) dv. \end{aligned} \tag{6}$$

To solve (6), we assume that data n_i's and the frequency ω are known and replace $\int_{t_i}^{t_i+\Delta t} \sin(\omega v) dv$ by $[\cos(\omega t_i) - \cos\{\omega(t_i + \Delta t)\}]/\omega$ and $\int_{t_i}^{t_i+\Delta t} \cos(\omega v) dv$ by $[\sin\{\omega(t_i + \Delta t)\} - \sin(\omega t_i)]/\omega$. The likelihood spectrum at ω is

$$S(\omega) = -\ln(\mathrm{GLR}) = \left[\sum_{i=1}^{N_t} \{n_i ln(\hat{\lambda}_i) - \hat{\lambda}_i\} - \ln(\hat{\lambda}_0 \Delta t) \sum_{i=1}^{N_t} n_i + N_t \hat{\lambda}_0 \Delta t \right], \tag{7}$$

where the expression of $\hat{\lambda}_i$ is given before Eq. (3). For a given value of ω, this is the key statistic used for the GLR test.

We can assume that the frequency ω is known or unknown when analyzing data. If ω is known and N_t is large, then to test the hypotheses (for detecting the signal), one can reject H_0 when $2S(\omega) > \chi^2_{2,\alpha}$, where $\chi^2_{2,\alpha}$ denotes the upper α percentile of the χ-square distribution with 2 degrees of freedom. For an unknown ω, we define the test statistic as

$$S_{\max} = \max_{\omega \in \Omega} S(\omega),$$

where Ω is set of set of M distinct frequencies. In this case, we reject H_0 when $S_{\max} > S_{\max,\alpha}$, where $S_{\max,\alpha}$ denotes the upper α percentile of the $S_{\max}$ distribution. Since the analytical form of the distribution is unknown, the percentile $S_{\max,\alpha}$ is determined by a numerical procedure given in the next section.

As an alternative to the GLR method, we also consider the Lomb-Scargle method [43], hereafter referred to as LS. The periodogram at a given frequency ω is

$$LS(\omega) = \frac{1}{2\sigma^2}\left(\frac{\left[\sum_{i=1}^{N_t} n_i \cos\{\omega(t_i-\tau)\}\right]^2}{\sum_{i=1}^{N_t}\cos^2\{\omega(t_i-\tau)\}} + \frac{\left[\sum_{i=1}^{N_t} n_i \sin\{\omega(t_i-\tau)\}\right]^2}{\sum_{i=1}^{N_t}\sin^2\{\omega(t_i-\tau)\}}\right)$$

with $\tau = (1/2\omega)\tan^{-1}\left\{\sum_{i=1}^{N_t}\sin(2\omega t_i)/\sum_{i=1}^{N_t}\cos(2\omega t_i)\right\}$ and $\sigma^2 = \sum_{i=1}^{N_t} n_i^2/(N_t-1)$. Like the GLR case, for known ω, we reject H_0 if $2L(\omega) > \chi^2_{2,\alpha}$ and for the unknown ω we reject H_0 if $L_{\max} = \max_{\omega\in\Omega} L(\omega) > L_{\max,\alpha}$. This $L_{\max,\alpha}$ is the upper α percentile point of $L_{\max}$. This percentile (or the critical value of this test) can be calculated analytically or numerically. Reference [34] approximated the distribution of $L_{\max}$ by the following probability density function:

$$f_X(x|\nu) = \nu(1-e^{-x})^{\nu-1}e^{-x}, \quad x > 0, \tag{8}$$

where ν is a function of the number of scanned frequencies in Ω. Following [37], we take $\nu = \mathcal{M}_{\text{scan}}$, and the details on how to calculate $\mathcal{M}_{\text{scan}}$ are given in the next section. To be specific, Eq. (8) is the density of the maximum of ν independent standard exponential ($\chi^2_2/2$) random variables. Therefore, we can determine the upper α percentile of $LS_{\max}$ from the density given in Eq. (8). The upper α percentile, denoted by $LS_{\max,\alpha,1}$ is $-\log\{1-(1-\alpha)^{1/\nu}\}$. We use $LS_{\max,\alpha,2}$ to denote the percentile determined by a simulation technique.

V. SYNTHETIC DATA SIMULATION STRATEGY

A. General simulation strategy

We generated data under H_0 and H_1. The counts n_i over the time bin $[t_i, t_i+\Delta t)$ follow:

$$\begin{array}{ll} \mathrm{Pois}\left\{(\mathcal{R}_s+\mathcal{R}_b)\mathcal{D}\Delta t\right\} & \text{under } H_0, \\ \mathrm{Pois}\left\{\mathcal{R}_b\mathcal{D}\Delta t + \mathcal{R}_s\mathcal{D}\left(\Delta t + A_d\int_{t_i}^{t_i+\Delta t}\sin\left(\frac{2\pi}{P}u-\Psi\right)du\right)\right\} & \text{under } H_1. \end{array}$$

Here, $\mathcal{R}_s$ is a constant signal event rate and $\mathcal{R}_b$ is a constant rate for the background noise. Here, we have chosen not to bin in recoil energy, so $\mathcal{R} = \mathcal{R}_s + \mathcal{R}_b$ denotes the event rate at any given time integrated over the entire recoil energy range and summing over all flux components. For analyzing (testing of hypotheses) simulated data, we employed the GLR and LS methods.

Note that we use a value of ω for data simulation. However, at the analyses stage, ω is assumed to be once known and then an unknown parameter. For unknown ω, the statistic $S_{\max}$ and the critical value of $S_{\max}$ are determined as follows. We take Ω as a set of $N_{\text{entire}} = n_o\mathcal{T}/\Delta t$ evenly spaced frequencies on the entire range for the scanned frequencies $[f_{\min}, 1/\Delta t]$ for a given run-time $\mathcal{T}$, width of the time interval Δt, and oversample factor n_o [44], so $\Omega = \{\omega_1, \ldots, \omega_{N_{\text{entire}}}\}$. We set $n_o = 10$ for the Monte Carlo simulation. We use the same Ω for both $S_{\max}$ and $L_{\max}$. Another concept needed for deriving the null distribution of $L_{\max}$ is the effective number of scanned frequencies over $[f_{\min}, 1/\Delta t]$. It is $\mathcal{M}_{\text{entire}} = N_{\text{entire}}/f_{\text{adj}}$, where f_{adj} is an empirical result for the scanning density. Note that we are interested in the frequency range $[f_{\min}, f_{\max}]$ with $f_{\max} = \min(1/\Delta t, 1\ \text{day}^{-1})$, and $f_{\min} = 1/365.25\ \text{day}^{-1}$ for $P = 1$ yr or 1 day, $f_{\min} = 1/11\ \text{yr}^{-1}$ for $P = 11$ yr. Then we overscan $N_{\text{entire}} \times f_{\text{scan}}/f_{\text{entire}}$ on $[f_{\min}, f_{\max}]$ where $f_{\text{entire}} = 1/\Delta t - f_{\min}$ and $f_{\text{scan}} = f_{\max} - f_{\min}$. Specifically, to be consistent with the frequency range of interest, f_{adj} for different Δt and $\mathcal{T}$ are shown in the Appendix. The number of independent frequencies scanned in a smaller frequency range [37] is $\mathcal{M}_{\text{scan}} = \mathcal{M}_{\text{entire}} \times f_{\text{scan}}/f_{\text{entire}}$, and this $\mathcal{M}_{\text{scan}}$ is used to approximate the distribution of $L_{\max}$ given in Eq. (8).

1. *Critical value $S_{\max,\alpha}$ from the distribution of $S_{\max}$*

We found that the empirical density of $S_{\max}$ is somewhat close to Eq. (8) for some choice of ν, which need not be the same as the number of frequencies of Ω. However, it is not easy to prove that the density of $S_{\max}$ has the form of Eq. (8) because (1) for any two arbitrary frequencies ω and ω', both $S(\omega)$ and $S(\omega')$ are calculated on the same observed data, just at two different frequencies, so they need not be independent, and (2) finding the distribution of the maximum of dependent χ^2 random variables is not an easy task. Therefore, the threshold $S_{\max,\alpha}$ estimated after fitting Eq. (8) to the $S_{\max}$ data will be an approximation of the upper α percentile of $S_{\max}$'s distribution. For each 5000 simulated dataset under H_0, we computed $S_{\max}$, which helps to obtain the empirical distribution of $S_{\max}$. We then fit model [Eq. (8)] to the $S_{\max}$ values denoted by $\{S_{\max,r}, r = 1, \ldots, 5000\}$ and obtain the maximum likelihood estimates (MLE) of ν by maximizing the following log-likelihood function:

$$\sum_{r=1}^{5000}\left[\log(\nu) + (\nu - 1)\log\{1 - \exp(-S_{\max,r})\} - S_{\max,r}\right].$$

Let us denote the MLE of ν by $\hat{\nu}$. Since the cumulative distribution function of the probability density [Eq. (8)] is $F(h) = \{1 - \exp(-h)\}^{\nu}$, we set $\{1 - \exp(-S_{\max,\alpha})\}^{\hat{\nu}} = 1 - \alpha$, and solving this equation we obtain the estimate $S_{\max,\alpha,1} = -\log\{1 - (1 - \alpha)^{1/\hat{\nu}}\}$. Next, we use the upper αth percentile of the 5000 $S_{\max}$ values as the second estimate of $S_{\max,\alpha}$, call it $S_{\max,\alpha,2}$.

2. Results between GLR and LS methods under H_0

In our simulation, we set $\alpha = 0.1$. The scanned frequencies were taken between $[f_{\min}, f_{\max}]$ with a bin width of Δt, run-time $\mathcal{T}$, and the detector size $\mathcal{D} = 100$ ton. Computation of the threshold under the Lomb-Scargle method was much faster as it did not involve any equation solving, even when the number of frequencies was on the order of 10^5. In contrast, the GLR-based approach was time consuming. Specifically, the computing time of GLR was proportional to the number of scanned frequencies and the length of n_i. We used scipy.root [45] and astropy.timeseries.LombScargle [46] of PYTHON for GLR and LS calculations, respectively. Table IV contains the critical values for the GLR and LS methods when $\mathcal{T} = 10$ yr.

3. Simulation procedure under H_1

The power of the test is the probability of rejecting H_0 when data are generated under the alternative hypothesis H_1. The simulated data under H_1 is a Poisson distribution with a time-varying rate determined by a given amplitude A_d and period P. We choose $\Psi = P/4$ such that the simulated time variation starts at the extreme value. In addition to studying signals with different periods, the knowledge of phase can be used to split the signals with the same period (dark matter yearly modulation and solar neutrino yearly modulation) but different amplitudes and phases, especially when one signal is well measured (solar neutrino) and the other signal is undetermined (dark matter).

In this work, we are mainly interested in the periodic signals in the neutrino flux from the Sun with a period of $P = 1$ day (due to Earth rotating itself), $P = 365.25$ days (due to Earth orbiting around the Sun), and atmosphere $P = 11$ yr (due to the 11 yr solar cycle, the changing strength of the solar wind). All three periods should, in principle, be observable. In the data generation process, we consider $P = 1$ day and 365.25 days with $\Delta t < 1$ day; $P = 365.25$ days with 1 day $\leq \Delta t < 365.25$ days; $P = 11$ yr when $\Delta t < 1$ yr and $\mathcal{T} \geq 11$ yr.

When $n_i \overset{ind}{\sim} \text{Poisson}(\lambda_i), i = 1, \ldots, N_t$, the power of the tests is calculated under two scenarios:

(1) Known period P: Under such cases when the periods are known, instead of searching for all possible physical and theoretical peaks by finding a peak as is being done in actual experiments, we calculate the statistics $S(\omega_{\text{known}})$ and $LS(\omega_{\text{known}})$ at that known $\omega_{\text{known}} = 2\pi/P$, instead of estimating ω. The powers of the tests are

$$\text{Power} = \begin{cases} pr\{2S(\omega_{\text{known}}) > \chi^2_{2,\alpha}\}, & \text{for GLR,} \\ pr\{2LS(\omega_{\text{known}}) > \chi^2_{2,\alpha}\}, & \text{for LS.} \end{cases}$$

(2) Unknown period P: Experimentally, possible periodic signals are searched by finding peaks over a

TABLE IV. This table shows the threshold values of the test statistic derived from (1) the Lomb-Scargle periodogram and (2) the GLR for different Δt, $\mathcal{T}$, $\mathcal{M}_{scan}$ and when the detector's size is assumed to be $\mathcal{D} = 100$ ton, $\mathcal{R}_s = 100$ ton^{-1} yr^{-1}, and $\mathcal{R}_b = 0$ ton^{-1} yr^{-1}, and $\alpha = 10\%$. The data are generated under H_0. Under each method two estimates of threshold are presented: (a) model based corresponds to the one with suffix 1 and (b) empirical distribution based corresponds to the one with suffix 2. All results are based on simulation with 5000 replications.

				LS			GLR		
$\mathcal{T}$ years	Δt days	$\mathcal{D}$ tons	Average number of events per bin	$\mathcal{M}_{\text{scan}}$	$LS_{\max,\alpha,1}$	$LS_{\max,\alpha,2}$	$\hat{\nu}$	$S_{\max,\alpha,1}$	$S_{\max,\alpha,2}$
10	30	100	821	202	7.56	7.24	133	7.14	7.39
10	10	100	273	608	8.66	8.4	463	8.39	8.49
10	5	100	136	1217	9.35	9.23	946	9.1	9.26
1/6	0.2	100	5	404	8.25	8.05	329	8.05	8.14
1/6	0.2	500	27	404	8.25	8.03	328	8.04	8.16
1/6	0.2	2000	109	404	8.25	8.12	325	8.03	8.22

wide frequency range. The scanned frequency range and frequency number are mentioned in the third paragraph of this section. In this case, $S_{\max}$ may be located at the alias of the input frequency instead of at the input frequency. The powers of the tests are

$$\text{Power} = \begin{cases} pr(S_{\max} > S_{\max,\alpha}), & \text{for GLR,} \\ pr(LS_{\max} > LS_{\max,\alpha}), & \text{for LS.} \end{cases}$$

We define $\beta = 1 - \text{Power}$ as the probability of failing to reject the null hypothesis when the alternative is true (i.e., the type-II error). For the empirical power (power obtained via simulation), we first fix $(\mathcal{R}_b, \mathcal{R}_s, \mathcal{D}, \mathcal{T}, P, \Psi, \Delta t)$. Then we change A_d over a grid of values. For every choice of $(\mathcal{R}_b, \mathcal{R}_s, \mathcal{D}, \mathcal{T}, P, \Psi, \Delta t, A_d)$, we generate Poisson data $\{n_1, \ldots, n_{N_t}\}$ under H_1. We calculate $S(\omega_{\text{known}})$ or $LS(\omega_{\text{known}})$ or $S_{\max}$ or $LS_{\max}$ for this simulated data. We repeat this procedure 5000 times, then calculate the proportion of times these quantities are larger than $\chi^2_{2,\alpha}$ or $S_{\max,\alpha}$ or $LS_{\max,\alpha}$ accordingly. This proportion is an estimate of the power [Eq. (9)]. This procedure is repeated for every combination of the parameters. Next we draw the power curves against A_d for a fixed value of $(\mathcal{R}_b, \mathcal{R}_s, \mathcal{D}, \mathcal{T}, P, \Psi, \Delta t)$ and we denote the amplitude A_d as $A_{d,\alpha,\beta}$ when the probability of type-I error rate of a hypothesis test being α and type-II error being β.

Figure 4 shows an example when the detecting period $P = 365.25$ days using the run-time $\mathcal{T} = 10$ yr and binned in $\Delta t = 0.2$, 10, 30 days. The left histograms are under the "known period" condition, where H_0 is the χ^2_2 distribution and H_1 is $2LS(\omega_{\text{known}})$. The right histograms are under the "unknown period" condition, where H_0 and H_1 are $LS_{\max}$. The amplitude for H_1 is $A_d = 0.024$. The vertical line in each panel is the critical value $\chi^2_{2,\alpha}$ (left column) and $LS_{\max,\alpha,1}$ (right column) when $\alpha = 0.1$. The power $(1 - \beta)$ is the proportion of $2LS(\omega_{\text{known}})$ (or $LS_{\max}$) greater than the threshold $\chi^2_{2,\alpha}$ (or $LS_{\max,\alpha,1}$) out of the 5000 realizations under H_1, where $\omega_{\text{known}} = 2\pi/P$.

4. Comparing $A_{d,\alpha,\beta}$ between GLR and LS methods

For a fixed value of $(\mathcal{R}_b, \mathcal{R}_s, \mathcal{D}, \mathcal{T}, P, \Psi, \Delta t)$, we want to compare $A_{d,\alpha,\beta}$ between LS and GLR methods, under known period and unknown period scenarios. We also test the performance for a small time bin and a small number of events [17]. For these purposes, we set $\mathcal{R}_s = 100$ and $\mathcal{R}_b = 0$ ton^{-1} yr^{-1}. We consider $\mathcal{T} = 1/6$ yr with $\Delta t = 0.2$ days, and $\mathcal{T} = 10$ yr with $\Delta t = 10$, 30 days and control the number of events in each time bin by changing $\mathcal{D}$. One example is shown in Fig. 5, and results are shown in Table V. Under the known period scenarios, the results from GLR and LS are similar. However, under the unknown period scenario, the power of GLR is generally better than the LS method, especially when the number of events in time bins is small. Both methods become equivalent in power as the number of events in each bin increases. We adopt LS in the rest of the analyses as it is computationally more efficient than GLR, especially for small time bin Δt and long run-time $\mathcal{T}$.

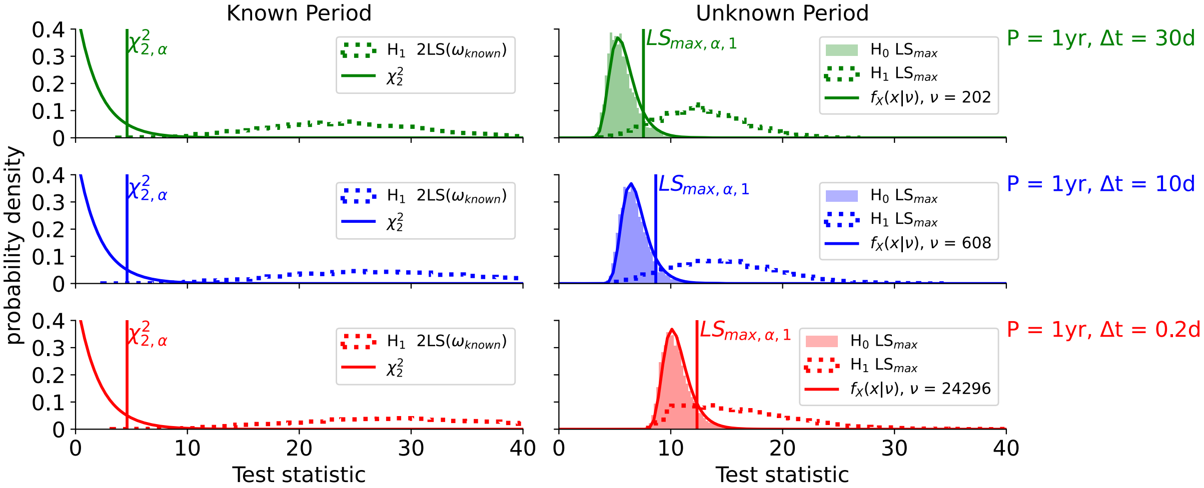

FIG. 4. Example of histograms for the assumptions of known periods (left) and unknown periods (right) under the null hypothesis H_0 and the alternative hypothesis H_1. Assumed parameters are run-time $\mathcal{T} = 10$ yr, time binnings $\Delta t = 0.2$, 10, 30 days, period of $P = 365.25$ days, amplitude $A_d = 0.024$, $\mathcal{R}_s = 100$ ton^{-1} yr^{-1}, and no experimental backgrounds $\mathcal{R}_b = 0$ ton^{-1} yr^{-1}. Left: the solid curve is the χ^2_2 distribution, the vertical line is the critical value $\chi^2_{2,\alpha}$ with $\alpha = 0.1$. The dotted histogram in each panel is the distribution of 5000 simulated values of $2LS_{\max}$ under the alternative hypothesis. Right: the filled histogram in each panel is the empirical distribution of 5000 simulated values of $LS_{\max}$ under the null hypothesis H_0 using the LS method as described in the text. The solid curve is $f_X(x|\nu)$ with $\nu = \mathcal{M}_{\text{scan}}$, the vertical line is the critical value $LS_{\max,\alpha,1}$ with $\alpha = 0.1$. The dotted histogram in each panel is the distribution of 5000 simulated values of $LS(\omega_{\text{known}})$ under the alternative hypothesis with $\omega_{\text{known}} = 2\pi/P$ at the detection period $P = 365.25$ days.

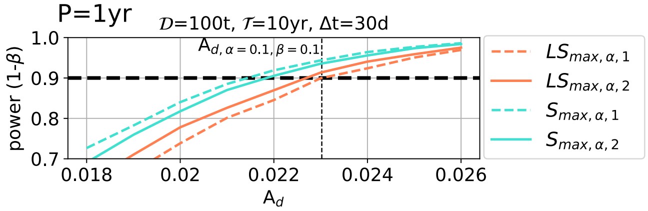

FIG. 5. Power curves (the probability of rejecting H_0) for the GLR and Lomb-Scargle methods when $\alpha = 0.1$ and $P = 1$ yr and under the unknown period scenario. The critical values are $LS_{\max,\alpha,1}$, $LS_{\max,\alpha,2}$ for LS and $S_{\max,\alpha,1}$ and $S_{\max,\alpha,2}$ for GLR. The vertical line is $A_{d,\alpha=0.1,\beta=0.1}$ under the LS method and when the critical value is $LS_{\max,\alpha,1}$.

B. Estimating $A_{d,\alpha,\beta}$ for arbitrary $(\mathcal{R}_s, \mathcal{R}_b, \mathcal{D})$ and fixed $(\mathcal{T}, \Delta t, P)$ via the signal-to-noise ratio

In the previous section, $A_{d,\alpha,\beta}$ is obtained via a simulation process for a given $(\mathcal{R}_b, \mathcal{R}_s, \mathcal{D}, \mathcal{T}, P, \Psi, \Delta t)$. This process is time intensive. It is desirable to obtain an analytical expression for the variation of $A_{d,\alpha,\beta}$ when $(\mathcal{R}_s, \mathcal{R}_b, \mathcal{D})$ take on different values. The signal rate $\mathcal{R}_s$ depends on flux uncertainty, $\sin\theta_w^2$, nuclei, physical process, energy threshold E_{thrd}, detector efficiency $\epsilon(E_r)$, and resolution $\sigma(E_r)$. The background rate $\mathcal{R}_b$ depends on the background depletion and physical process to generate the background. The detector size $\mathcal{D}$ depends on the experiment. In this section, after obtaining $A_{d,\alpha,\beta}$ for $(\mathcal{R}_b, \mathcal{R}_s, \mathcal{D}, \mathcal{T}, P, \Psi, \Delta t)$, we find an efficient way to obtain $A'_{d,\alpha,\beta}$ for $(\mathcal{R}'_b, \mathcal{R}'_s, \mathcal{D}', \mathcal{T}, P, \Psi, \Delta t)$ so that the test maintains the same power.

We set $\alpha = 0.1$ and $(1-\beta) = 0.9$ for the "90% detection," then the corresponding detectable amplitude is denoted by $A_{d,\alpha=0.1,\beta=0.1}$. The signal for the detectable amplitude $A_{d,\alpha,\beta}$ in the time bin $[t_i, t_i+\Delta t]$ under H_1 is $\mathcal{R}_s \mathcal{D} A_{d,\alpha,\beta} \int_{t_i}^{t_i+\Delta t} \sin(2\pi u/P)du$. Here α, β, P, Δt, and $\mathcal{T}$ are assumed to be fixed (not changing). Also, the background is $\sqrt{(\mathcal{R}_s+\mathcal{R}_b)\mathcal{D}\Delta t}$, representing the Poisson standard deviation under the null model for the number of occurrences in one interval. Since the time-dependent parameters ($\mathcal{T}$, Δt, P) are fixed, the critical value stays the same during the scaling. In addition, the signal function deviated from the background on interval $[t_i, t_i+\Delta t]$ is $A_{d,\alpha,\beta}\mathcal{R}_s\mathcal{D}\int_{t_i}^{t_i+\Delta t}\sin(2\pi u/P)du$. The component $\int_{t_i}^{t_i+\Delta t}\sin(2\pi u/P)du$ determines the shape of the signal on $[0, T]$. When time-dependent parameters ($\mathcal{T}$, Δt, P) are fixed, the shape of this signal function over $[0, \mathcal{T}]$ may remain the same, but its magnitude may be different, depending on the parameters ($A_{d,\alpha,\beta}$, $\mathcal{R}_s$, $\mathcal{D}$). In this case, the power of the tests only depends on the signal's magnitude, because the shape's effect is the same. The squared signal-to-noise ratio (SNR^2) is

$$\mathrm{SNR}^2|_{\mathcal{R}_s,\mathcal{R}_b,\mathcal{D}} = A^2_{d,\alpha,\beta} \times \mathcal{R}_s \times \mathcal{D} \times \frac{1}{(1+\mathcal{R}_b/\mathcal{R}_s)} \times F(P, \mathcal{T}, \Delta t),$$

where $F(P, \mathcal{T}, \Delta t)$ contains parameters only describing time information of the signal and is some suitable effect due to the shape on the squared signal-to-noise ratio. Note that the signal-to-noise ratio for amplitude $A_{d,\alpha,\beta}$ when there is no constant background $(\mathcal{R}_s, \mathcal{R}_b = 0, \mathcal{D})$ is

$$\mathrm{SNR}^2|_{\mathcal{R}_s,\mathcal{R}_b=0,\mathcal{D}} = A^2_{d,\alpha,\beta} \times \mathcal{R}_s \times \mathcal{D} \times F(P, \mathcal{T}, \Delta t).$$

Therefore, for any $(\mathcal{R}_s, \mathcal{R}_b, \mathcal{D})$,

$$\mathrm{SNR}^2|_{\mathcal{R}_s,\mathcal{R}_b=0,\mathcal{D}} = \mathrm{SNR}^2|_{\mathcal{R}_s,\mathcal{R}_b>0,\mathcal{D}} \times \left(1+\frac{\mathcal{R}_b}{\mathcal{R}_s}\right). \quad (9)$$

Next,

TABLE V. This table shows the amplitude $A_{d,\alpha,\beta}$ when $\alpha = 0.1$, $\beta = 0.1$ for scenarios (1) known period and (2) unknown period and methods (1) the Lomb-Scargle periodogram and (2) the GLR, for different $\mathcal{D}$, $\mathcal{T}$, Δt and when $\mathcal{R}_s = 100$, $\mathcal{R}_b = 0$ ton^{-1} yr^{-1}. Under the known period scenario, the critical value is $\chi^2_{2,\alpha}$ for LS and GLR. Under the unknown period scenario, the critical values are $LS_{\max,\alpha,1}$, $LS_{\max,\alpha,2}$ for LS and $S_{\max,\alpha,1}$ and $S_{\max,\alpha,2}$ for GLR.

					$A_{d,\alpha,\beta}$					
					Known period scenario		Unknown period scenario			
$\mathcal{T}$ years	Δt days	Period days	$\mathcal{D}$ tons	Average number of events per bin	LS	GLR	$LS_{\max,\alpha,1}$	$LS_{\max,\alpha,2}$	$S_{\max,\alpha,1}$	$S_{\max,\alpha,2}$
10	30	365.25	100	821	0.015	0.015	0.023	0.023	0.021	0.022
10	10	365.25	100	273	0.015	0.015	0.023	0.023	0.023	0.023
1/6	0.2	1	100	5	0.12	0.12	0.195	0.193	0.188	0.189
1/6	0.2	1	500	27	0.055	0.054	0.087	0.086	0.084	0.084
1/6	0.2	1	2000	109	0.027	0.027	0.043	0.043	0.042	0.042

$$\begin{aligned}\text{SNR2}|_{\mathcal{R}_s,\mathcal{R}_b=0,\mathcal{D}} &= A^2_{d,\alpha,\beta}\times\mathcal{R}_s\times\mathcal{D}\times F(P,\mathcal{T},\Delta t)\\ &= A^2_{d,\alpha,\beta}\times\mathcal{R}_s\left(\frac{\mathcal{R}'_s}{\mathcal{R}'_s}\right)\times\mathcal{D}\left(\frac{\mathcal{D}'}{\mathcal{D}'}\right)\\ &\quad\times F(P,\mathcal{T},\Delta t)\\ &= \left(A_{d,\alpha,\beta}\sqrt{\frac{\mathcal{R}_s}{\mathcal{R}'_s}}\sqrt{\frac{\mathcal{D}}{\mathcal{D}'}}\right)^2\times\mathcal{R}'_s\times\mathcal{D}'\\ &\quad\times F(P,\mathcal{T},\Delta t).\end{aligned}\tag{10}$$

Now, suppose that for another set of values of $(\mathcal{R}'_s, \mathcal{R}'_b = 0, \mathcal{D}')$ the signal-to-noise ratio is the same as for $(\mathcal{R}_s, \mathcal{R}_b = 0, \mathcal{D})$ while all other parameters except the amplitude are fixed for both cases, i.e.,

$$\begin{aligned}\text{SNR}^2|_{\mathcal{R}'_s,\mathcal{R}'_b=0,\mathcal{D}'} &= A'^2_{d,\alpha,\beta}\times\mathcal{R}'_s\times\mathcal{D}'\times F(P,\mathcal{T},\Delta t)\\ &= \text{SNR}^2|_{\mathcal{R}_s,\mathcal{R}_b=0,\mathcal{D}}.\end{aligned}\tag{11}$$

Now, using Eqs. (9) and (11) we obtain

$$\begin{aligned}\text{SNR}^2|_{\mathcal{R}'_s,\mathcal{R}'_b>0,\mathcal{D}'}\times\left(1+\frac{\mathcal{R}'_b}{\mathcal{R}'_s}\right) &= \text{SNR}^2|_{\mathcal{R}'_s,\mathcal{R}'_b=0,\mathcal{D}'}\\ &= \text{SNR}^2|_{\mathcal{R}_s,\mathcal{R}_b=0,\mathcal{D}},\end{aligned}\tag{12}$$

and using Eqs. (10) in (12) we have

$$\begin{aligned}&(A'_{d,\alpha,\beta})^2\times\mathcal{R}'_s\times\mathcal{D}'\times\frac{1}{(1+\mathcal{R}'_b/\mathcal{R}'_s)}\times F(P,\mathcal{T},\Delta t)\\ &\quad=\left(A_{d,\alpha,\beta}\sqrt{\frac{\mathcal{R}_s}{\mathcal{R}'_s}}\sqrt{\frac{\mathcal{D}}{\mathcal{D}'}}\right)^2\times\mathcal{R}'_s\times\mathcal{D}'\times F(P,\mathcal{T},\Delta t),\end{aligned}$$

which yields the amplitude for other setting $(\mathcal{R}'_s, \mathcal{R}'_b = 0, \mathcal{D}')$,

$$A'_{d,\alpha,\beta} = A_{d,\alpha,\beta}\times\sqrt{\frac{\mathcal{R}_s}{\mathcal{R}'_s}}\sqrt{\frac{\mathcal{D}}{\mathcal{D}'}}\times\sqrt{1+\frac{\mathcal{R}'_b}{\mathcal{R}'_s}}.\tag{13}$$

As an example, for $\mathcal{T} = 10$ yr, $\Delta t = 10$ days, $P = 365.25$ days, $\mathcal{R}_s = 100\ \text{ton}^{-1}\ \text{yr}^{-1}$, $\mathcal{R}_b = 0\ \text{ton}^{-1}\ \text{yr}^{-1}$, and $\mathcal{D} = 100$ ton, the detectable amplitude with a power of 90% and a level of significance 10% is $A_{d,\alpha=0.1,\beta=0.1} = 0.02357377$ (results in Fig. 5). Using Eq. (13), we can now obtain the detectable amplitude $A'_{d,\alpha=0.1,\beta=0.1} = 0.1292$ for $\mathcal{D}' = 100$ ton, $\mathcal{R}'_s = 474.367\ \text{ton}^{-1}\ \text{yr}^{-1}$ (ES xenon resolution + efficiency), and $\mathcal{R}'_b = 50060.5\ \text{ton}^{-1}\ \text{yr}^{-1}$ (all backgrounds). This calculation is done without running a time-consuming simulation. The detectable amplitudes for other possible values of $\mathcal{R}'_s$ and $\mathcal{R}'_b$ are given in the "signal components" and "background components" column in Tables I and II. Moreover, when the eccentricity $A'_{d,\alpha=0.1,\beta=0.1} = A_{ecc} = 0.03342$, using Eq. (13) we obtain the detector's size $\mathcal{D}'$,

$$\mathcal{D}' = \mathcal{D}\left(A_{d,\alpha=0.1,\beta=0.1}\times\frac{\sqrt{1+\mathcal{R}'_b/\mathcal{R}'_s}}{A_{ecc}}\right)^2\left(\frac{\mathcal{R}_s}{\mathcal{R}'_s}\right),$$

interpreted as the detector size required for the eccentricity to be 90% detected.

Further estimations for different ($\mathcal{T}$, Δt, P) are derived from Figs. 6 and 7. Figures 8 and 9 show the amplitudes for different combinations of $(\mathcal{T}, \Delta t, P, \alpha, \beta)$. For example, running simulations we obtain $A_{d,\alpha=0.1,\beta=0.1} = 0.0291161$, $A_{d,\alpha=0.05,\beta=0.1} = 0.03$ for $\mathcal{T} = 10$ yr, $\Delta t = 0.2$ days, $P = 1$ day, $\mathcal{R}_s = 100\ \text{ton}^{-1}\ \text{yr}^{-1}$, $\mathcal{R}_b = 0\ \text{ton}^{-1}\ \text{yr}^{-1}$, $\mathcal{D} = 100$ ton. Then using Eq. (13) we obtain $A'_{d,\alpha=0.1,\beta=0.1}$, $A'_{d,\alpha=0.05,\beta=0.1}$ for the same $\mathcal{T}$, Δt, P and different choices of $(\mathcal{R}'_s, \mathcal{R}'_b, \mathcal{D}')$. We also consider the cases ($\mathcal{T} = 10$ yr, $\Delta t = 0.2$ days, $P = 1$ day), ($\mathcal{T} = 10$ yr, $\Delta t = 10$ days, $P = 1$ yr), and ($\mathcal{T} = 10$ yr, $\Delta t = 30$ days, $P = 1$ yr).

C. Estimating $A_{d,\alpha,\beta}$ to have the required power with different Δt and $\mathcal{T}$

We now fix $\mathcal{R}_s = 100\ \text{ton}^{-1}\ \text{yr}^{-1}$, $\mathcal{R}_b = 0\ \text{ton}^{-1}\ \text{yr}^{-1}$, $\mathcal{D} = 100$ ton and explore the relation between the amplitude $A_{d,\alpha,\beta}$ and the time-dependent parameters $(\mathcal{T}, \Delta t, P)$. For a given $(\mathcal{T}, \Delta t)$, we scan a series of frequencies (P) to obtain $A_{d,\alpha,\beta,P}$ for each P. Then we find the P range where $A_{d,\alpha,\beta}$ is roughly constant $A_{d,\alpha,\beta,P} \approx \bar{A}_{d,\alpha,\beta}$ where we use $\bar{A}_{d,\alpha,\beta}$ to denote the average of the amplitudes over different Ps.

The simulations show how different T and Δt affect the strength of signal $A_{d,\alpha,\beta}$ to maintain 90% power of the test. With the requirement that $P \gg \Delta t$, $\int_{t_i}^{t_i+\Delta t}\sin(\omega v)dv \approx \Delta t\sin(\omega t_i)$. Therefore, when $\mathcal{R}_b = 0$, the signal-to-noise ratio $\text{SNR}^2_{\mathcal{R}_s,\mathcal{R}_b=0,\mathcal{D}}$ is approximated by $A^2_{d,\alpha,\beta}\times\mathcal{R}_s\times\mathcal{D}\times\Delta t\times F_{\sin}(\mathcal{T}, P)$, where $F_{\sin}(\mathcal{T}, P)$ represents the effect on the signal-to-noise ratio due to different parameters T and P, considering a signal with the shape of $\sin(\omega t)$. The sample size of observations is $N_t = T/\Delta t$. The sample can differ with $\mathcal{T}$ and Δt. When all other parameters are fixed, but Δt decreases, the signal-to-noise ratio decreases, while the sample size N_t increases. Consequently, the expected power shall remain the same.

The simulation results showing how $A_{d,\alpha,\beta}$ depends on different parameters as a function of P are given in Figs. 6 and 7. Each panel is the $A_{d,\alpha=0.1,\beta=0.1,P}$ for a series of scanned frequencies (P) under a given $(\mathcal{T}, \Delta t)$. $A_{d,\alpha=0.1,\beta=0.1,P}$ is roughly constant when Δt is small enough such that the reached A_d is the same as the input A_d, $10\Delta t < P < \mathcal{T}/4$ when $\Delta t \geq 10$ days and $20\Delta t < P < \mathcal{T}/4$ when $\Delta t < 10$ days. In addition, we found an interesting empirical relationship that by an equation $y = ax^2 + bx + c$, where $y = \log(\bar{A}^2_{d,\alpha,\beta}\mathcal{R}_s\mathcal{D}\Delta t)$ and x

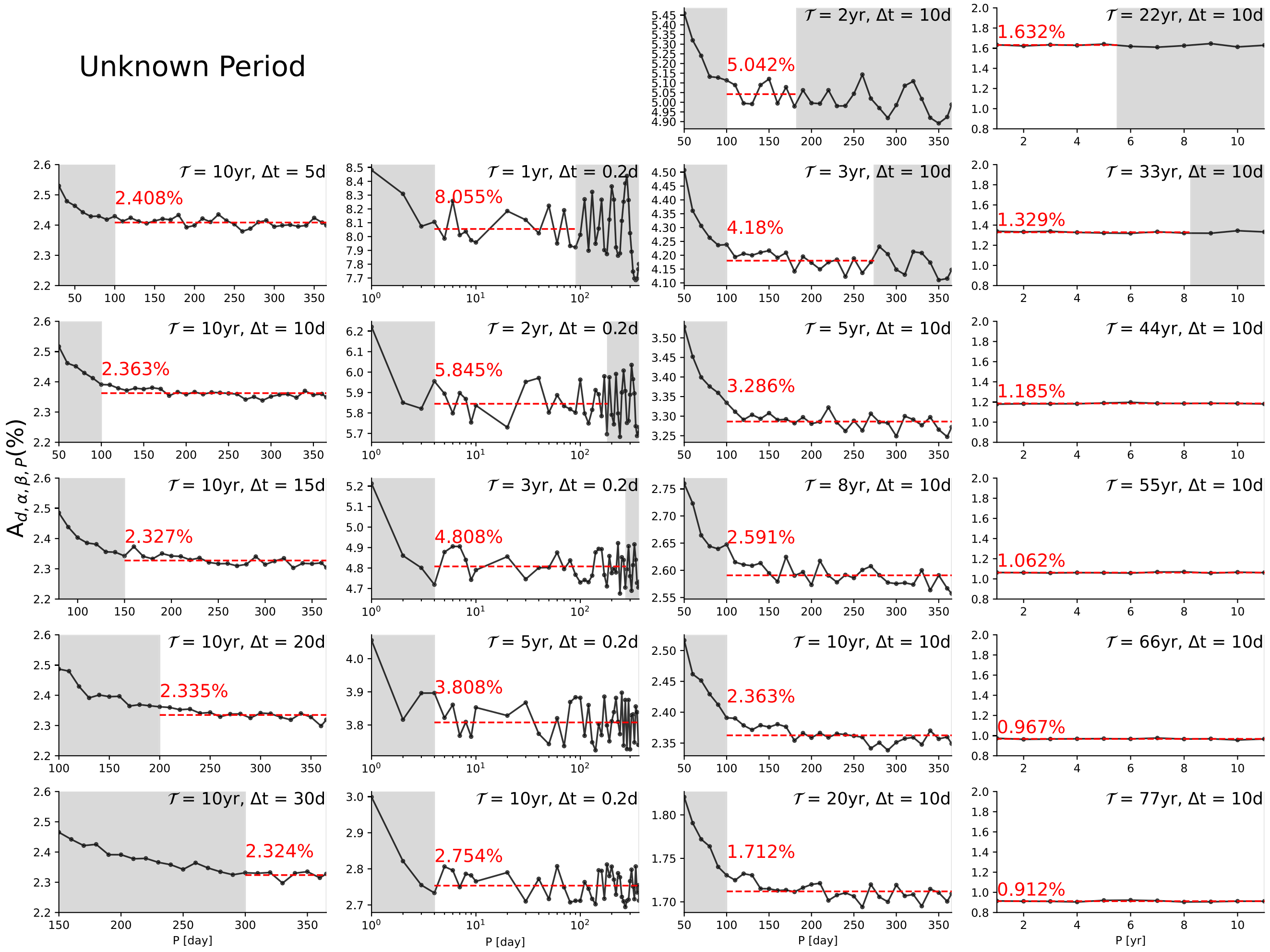

FIG. 6. The unknown period scenario plot for 90% detection ($\alpha = 0.1$, $\beta = 0.1$) amplitude $A_{d,\alpha,\beta,P}$ as a function of P for different ($\mathcal{T}$, Δt) and when $\mathcal{R}_s = 100\ \mathrm{ton}^{-1}\ \mathrm{yr}^{-1}$, $\mathcal{R}_b = 0\ \mathrm{ton}^{-1}\ \mathrm{yr}^{-1}$, and $\mathcal{D} = 100$ ton in the simulation study. First column: $\mathcal{T} = 10$ yr, Δt varies from 5 to 30 days. Second column: $\Delta t = 0.2$ days and $\mathcal{T}$ varies from 1 to 10 yr. Third column: $\Delta t = 10$ days and $\mathcal{T}$ varies from 2 to 20 yr. Fourth column: $\Delta t = 10$ days and $\mathcal{T}$ varies from 22 to 77 yr. In each panel, the white region is where the amplitude $A_{d,\alpha,\beta,P}$ can be approximated by the average of the amplitudes over different frequencies $\bar{A}_{d,\alpha,\beta}$, and the red horizontal line is $\bar{A}_{d,\alpha,\beta}$.

depends on the sample size of observation N_t and the critical value. Specifically, $x = \log\{\tau(\mathcal{M}_{\mathrm{scan}})/N_t\}$, where $\tau(\mathcal{M}_{\mathrm{scan}}) = \max(1, \log(\mathcal{M}_{\mathrm{scan}}))$. Under the known period scenario, $\mathcal{M}_{\mathrm{scan}} = 1$ and $x = \log(1/N_t)$. For a given α, the critical value is constant under the known period scenario, and for the unknown period scenario, with $\mathcal{M}_{\mathrm{scan}} \gg 1$, the critical value $LS_{\max,\alpha,2} \approx CONST + \log(M_{\mathrm{scan}})$. The corresponding x and the fitted a, b, c for different parameters are showed in Table VI.

Using the above empirical relations, to summarize the procedure to find $A_{d,\alpha,\beta}$, first, we select the proper Δt and $\mathcal{T}$ based on possible P such that $A_{d,\alpha,\beta,P} \approx \bar{A}_{d,\alpha,\beta}$. Adjust $\mathcal{M}_{scan}$ such that $LS_{\max,\alpha,1} \approx LS_{\max,\alpha,2}$ to ensure H_0 is consistent with the model and obtain $\mathcal{M}_{scan}$ and x, then obtain $\bar{A}_{d,\alpha,\beta} = \sqrt{\frac{e^{ax^2+bx+c}}{\mathcal{R}_s \mathcal{D} \Delta t}}$ using parameters in Table VI and obtain

$$\bar{A}'_{d,\alpha,\beta} = \bar{A}_{d,\alpha,\beta} \times \sqrt{\frac{\mathcal{R}_s}{\mathcal{R}'_s}} \sqrt{\frac{\mathcal{D}}{\mathcal{D}'}} \sqrt{1 + \frac{\mathcal{R}'_b}{\mathcal{R}'_s}} \tag{14}$$

via Eq. (13). Then, the nearby amplitudes are scanned for more accurate simulations. The detector size $\mathcal{D}'$ can be obtained similarly via $\mathcal{D}' = \mathcal{D} \times \left(\frac{\bar{A}_{d,\alpha,\beta}}{A_{ecc}}\right)^2 \frac{\mathcal{R}_s}{\mathcal{R}'_s}\left(1 + \frac{\mathcal{R}'_b}{\mathcal{R}'_s}\right)$.

While Fig. 10 shows how the power increases with the run time $\mathcal{T}$ under fixing α and fixing amplitude, Figs. 11, 13, and 15 are the application of this method and show what amplitude needs to be under different run time $\mathcal{T}$ to reach a fixing power and fixing α to estimate $\bar{A}'_{d,\alpha=0.1,\beta=0.1}$ as a function of run-time $\mathcal{T}$. We choose $\Delta t = 0.05$ days for $P = 1$ day, and $\Delta t = 10$ days for $P = 1$ and 11 yr, such that $A'_{d,\alpha,\beta,P} \approx \bar{A}'_{d,\alpha,\beta}$ for these periods. The minimum run-time $\mathcal{T}$ when $\bar{A}'_{d,\alpha=0.1,\beta=0.1}$ meets $A_{ecc} = 0.03342$ or $A_{d,DN,\max} = 0.00891$ or A_{atm} can be interpreted as the above physical

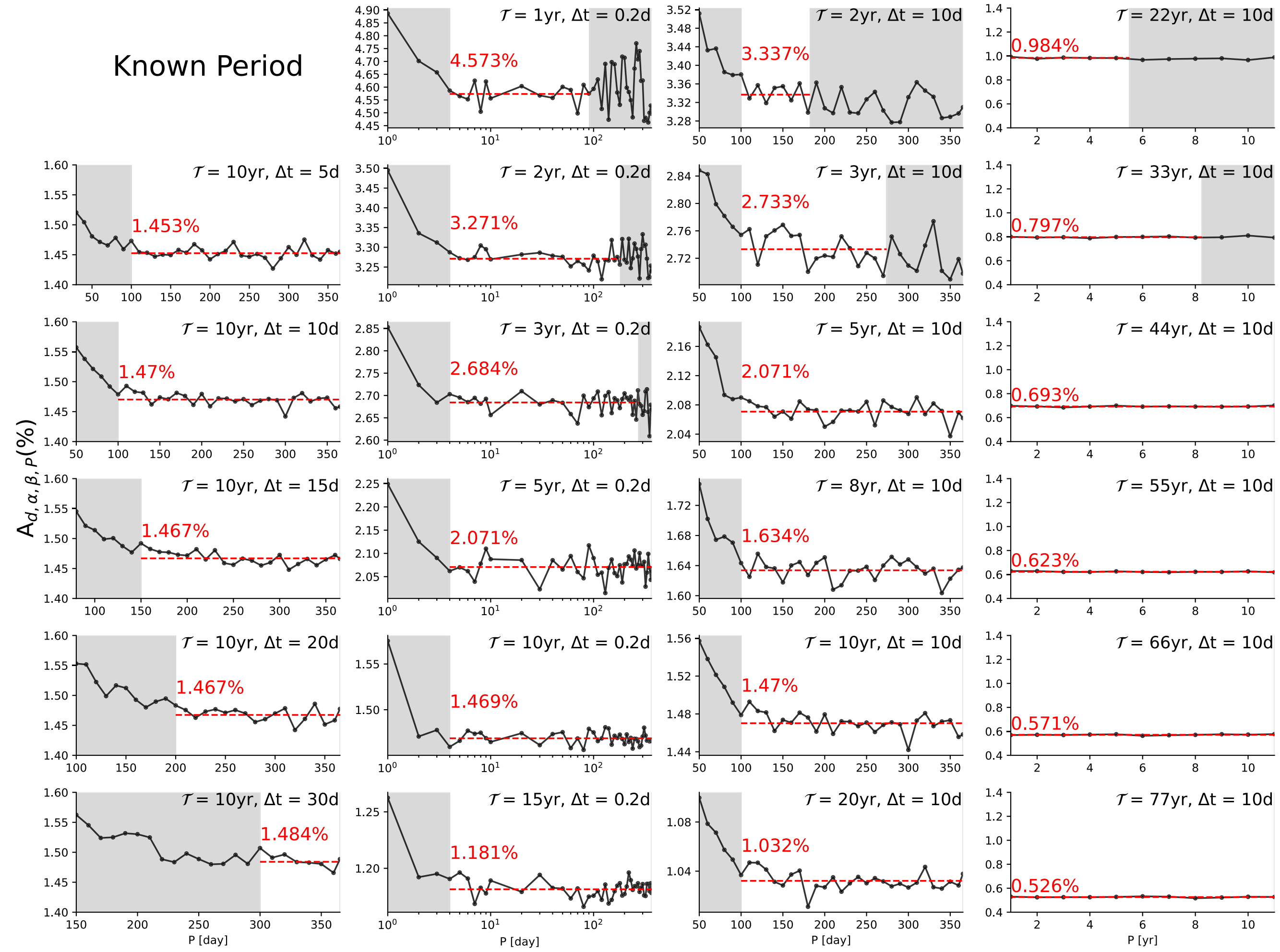

FIG. 7. Same as Fig. 6 but for known periods.

amplitudes are the 90% detectable amplitudes. Though the empirical results are fitting within $[x_{\min}, x_{\max}]$, the results from simulating the nearby run-time $\mathcal{T}$ is consistent with these estimated $\mathcal{T}$ when $x < x_{\min}$ or $x > x_{\max}$.

VI. RESULTS

We now move on to presenting the results for the time-varying analysis, focusing first on solar neutrinos. As above, we consider the electron neutrino scattering channel (ES) and nuclear recoil channels (CEνNS) separately, and the results are split into known period and unknown period scenarios. Starting with the ES channel, we take the end point energy of ^{7}Be and calculate $R_\odot$ in Eq. (1) by summing all the components of the solar neutrino flux (pp, CNO, ^{7}Be, and pep) over a range [1 keV, 650 keV] for the ideal resolution + ideal efficiency case and [0 keV, 790 keV] for the smear + efficiency case, since the contribution outside of this range is dominated by $2\nu\beta\beta$. The flux within these ranges is dominated by pp neutrinos.

We first show the results as a function of different depletion of backgrounds for ES and as a function of different energy thresholds for CEνNS, under the fiducial

TABLE VI. Fitted values of a, b, c for the empirical relationship $y = ax^2 + bx + c$ within $[x_{\min}, x_{\max}]$ assuming $\mathcal{R}_s = 100$ ton^{-1} yr^{-1}, $\mathcal{R}_b = 0$, $\mathcal{D} = 100$ ton.

	$x_{\min}$	$x_{\max}$	α	β	a	b	c
Known period	−10.218	−4.291	0.1	0.1	3.004×10^{-3}	1.049	3.251
			0.05	0.1	5.168×10^{-3}	1.077	3.529
Unknown period	−7.5	−2.755	0.1	0.1	2.344×10^{-2}	1.309	3.037
			0.05	0.1	2.598×10^{-2}	1.345	3.224

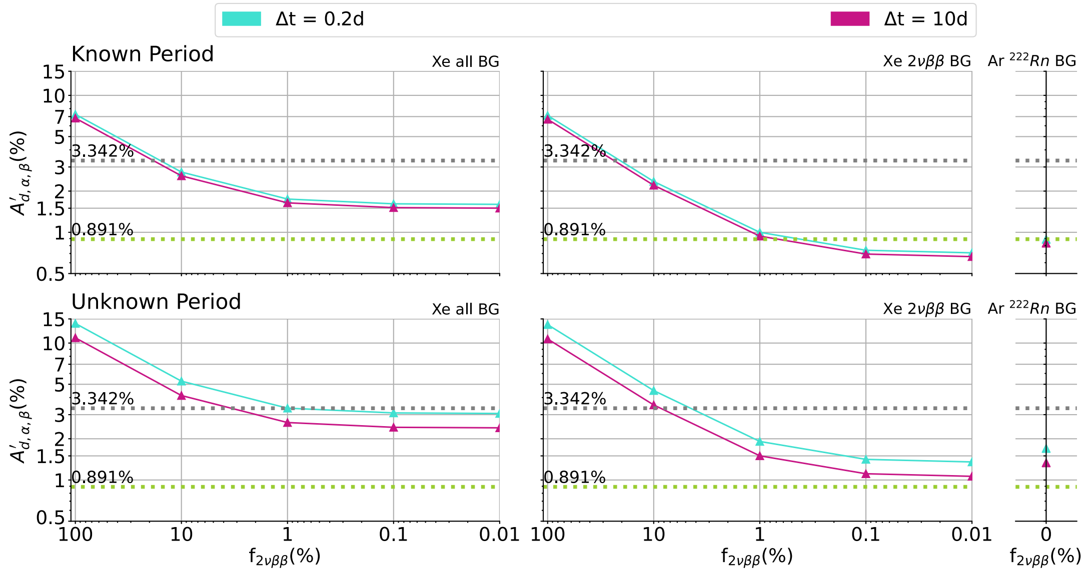

FIG. 8. 90% detection ($\alpha = 0.1$, $\beta = 0.1$) amplitude $A'_{d,\alpha,\beta}$ for solar components through electron scattering obtained from Eq. (13) as a function of $2\nu\beta\beta$ fraction $f_{2\nu\beta\beta}$. The top horizontal dashed line shows the expected amplitude due to the eccentricity $A_{ecc} = 0.03342$ and the bottom horizontal line shows the bound on the amplitude of the day-night modulation from Borexino $A_{d,DN,\max} = 0.00891$. The label "BG" indicates "background components" and "allBG" includes $2\nu\beta\beta$, ^{222}Rn, and ^{85}Kr backgrounds. The assumed run-time is $\mathcal{T} = 10$ yr, and the detector size $\mathcal{D} = 100$ ton. The time binnings and periods are $\Delta t = 0.2$ days for $P = 1$ day, $\Delta t = 10$ days for $P = 1$ yr. The curves show the spectrum including energy resolution and Xe100t-5 detector efficiency for xenon (Fig. 3) and 10% energy resolution with recoil energy threshold 100 keV only for argon. Each curve is for a different time binning Δt, as indicated.

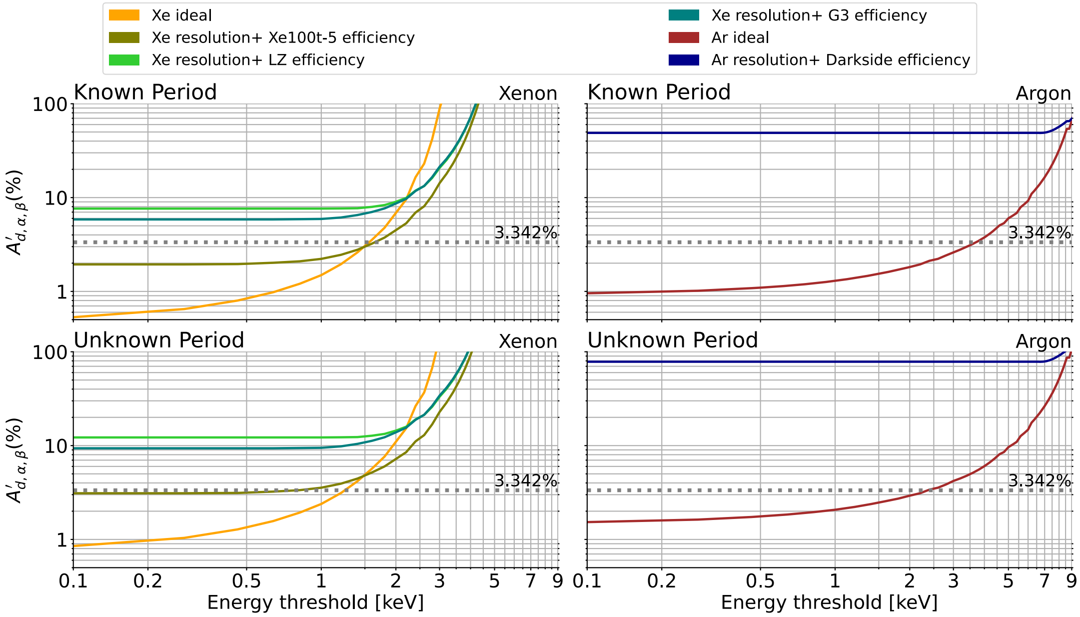

FIG. 9. 90% detection ($\alpha = 0.1$, $\beta = 0.1$) amplitude $A'_{d,\alpha,\beta}$ for ^{8}B solar components through CEνNS obtained from Eq. (13) as a function of recoil energy threshold, using $\Delta t = 10$ days. The assumed run-time is $\mathcal{T} = 10$ yr, and the detector size is $\mathcal{D} = 100$ ton. Curves are shown for different detector and efficiency models as indicated. The dashed line is the amplitude of yearly modulation $A_{ecc} = 0.03342$.

case of a 100-ton detector, with a run-time of ten years and a fixed time-bin Δt (Figs. 8 and 9). Then we show the results as a function of detector run-time for a fixed time bin Δt, detector size $\mathcal{D}$ for ES and CEνNS (Figs. 10–15).

Figure 8 shows the required amplitude at which the probability of detecting the signal is $1-\beta = 0.9$, at $\alpha = 0.1$. Indicated on the figure as the upper horizontal line is the modulation amplitude induced by the eccentricity.

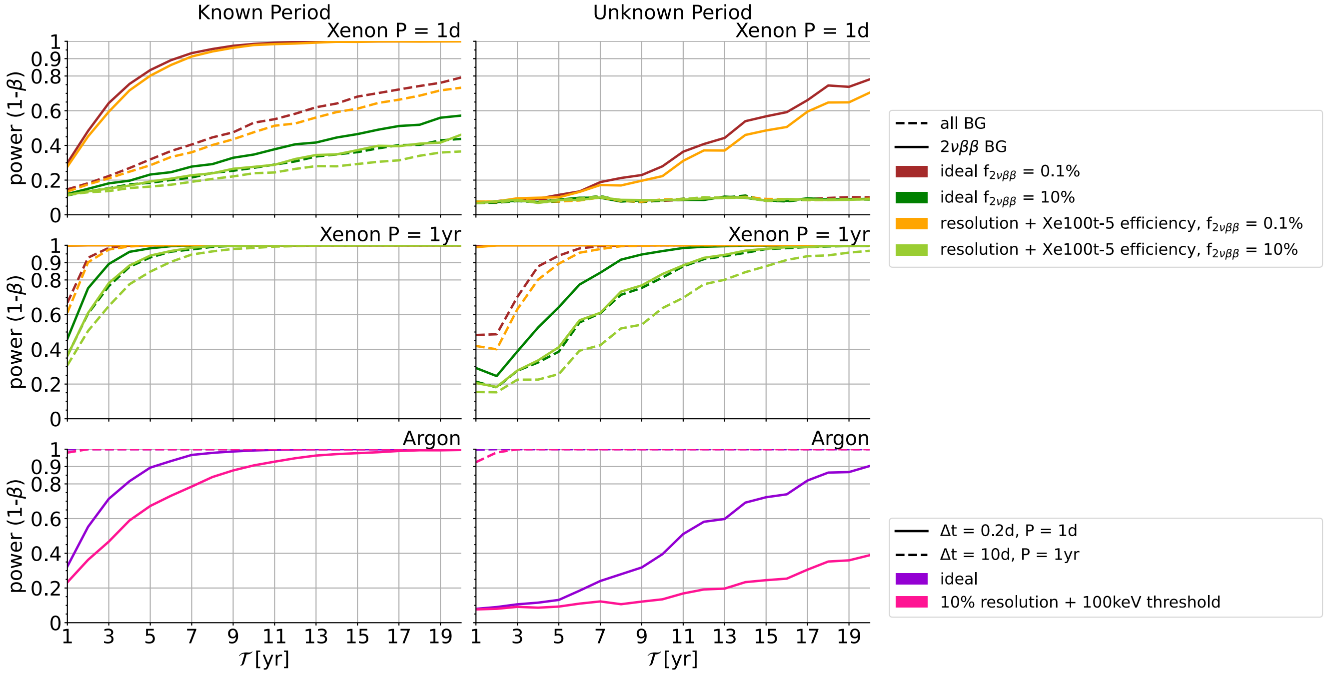

FIG. 10. The power for detecting time variation of solar components (summing over pp, ^{7}Be, CNO, and pep components) through electron scattering, under the assumption of the known period (left) and unknown period (right) scenarios described in the text. We take $\alpha = 0.1$ and plot the results as a function of detector run-time $\mathcal{T}$. The yearly modulation has an amplitude of $A_{ecc} = 0.03342$, due to the eccentricity of Earth's orbit, and the daily modulation has an amplitude of $A_{d,DN,\mathrm{max}} = 0.00891$, which matches the Borexino upper limits on the daily modulation. The assumed detector size is $\mathcal{D} = 100$ ton. Top row: xenon detection of $A_{d,DN,\mathrm{max}}$ for a time binning of $\Delta t = 0.2$ days. Middle row: xenon detection of A_{ecc} with $\Delta t = 10$ days. Bottom row: argon detection of A_{ecc} with $\Delta t = 10$ days, and $A_{d,DN,\mathrm{max}}$ with $\Delta t = 0.2$ days. For xenon, all BG includes $2\nu\beta\beta$, ^{222}Rn, and ^{85}Kr. For argon, the background includes ^{222}Rn.

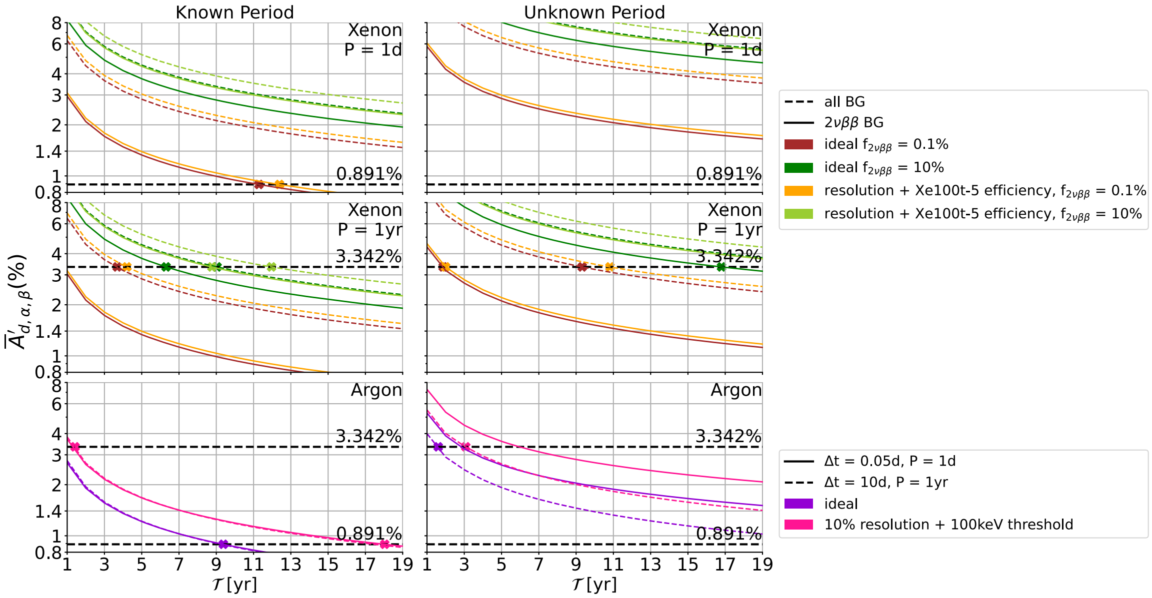

FIG. 11. The detectable amplitude for solar components through electron scattering with 90% power and 10% level of significance ($\alpha = 0.1, \beta = 0.1$), estimated from Eq. (14) as a function of detector run-time $\mathcal{T}$ for $\mathcal{D}' = 50$ ton, under known period and unknown period scenarios. Dashed lines are the amplitude of yearly modulation $A_{ecc} = 0.03342$ and the day-night modulation $A_{d,DN,\mathrm{max}} = 0.00891$. Top row: xenon detection of $A_{d,DN,\mathrm{max}}$ for a time binning of $\Delta t = 0.05$ days. Middle row: xenon detection of A_{ecc} with $\Delta t = 10$ days. Bottom row: argon detection of A_{ecc} with $\Delta t = 10$ days and of $A_{d,DN,\mathrm{max}}$ with $\Delta t = 0.05$ days. Points indicate the run-time $\mathcal{T}$ when $\bar{A}'_{d,\alpha=0.1,\beta=0.1}$ reaches A_{ecc} or $A_{d,DN,\mathrm{max}}$. For xenon, all BG includes $2\nu\beta\beta$, ^{222}Rn, and ^{85}Kr. For argon, the background includes ^{222}Rn.

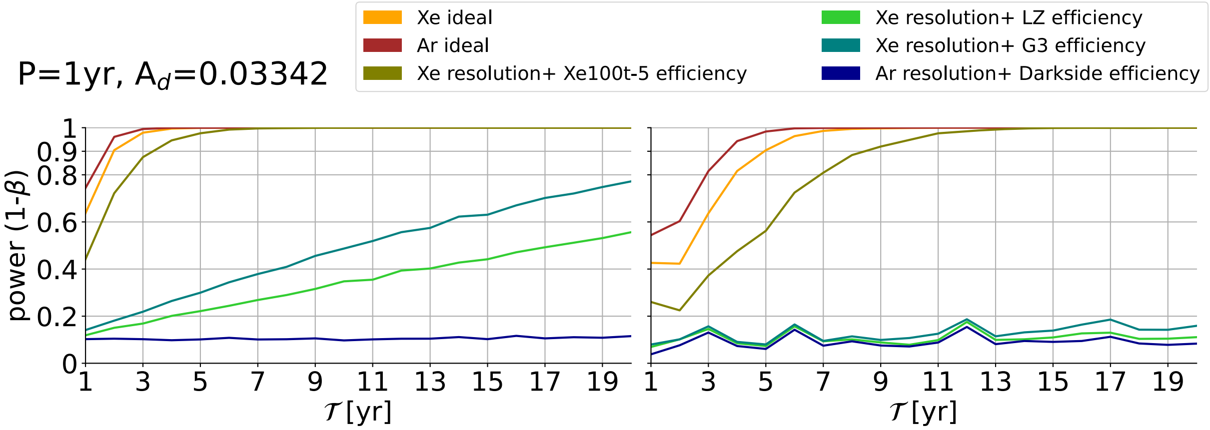

FIG. 12. The power of detecting time variation of ^{8}B through CEνNS under known period (left column) and unknown period (right column) scenarios with $\alpha = 0.1$, as a function of detector run-time $\mathcal{T}$. The assumed detector size is 100 ton. For xenon, assumptions are for an ideal detector and the Xe100t-5, LZ, and G3 detector efficiencies, and for argon, an ideal detector and the Darkside detector efficiency.

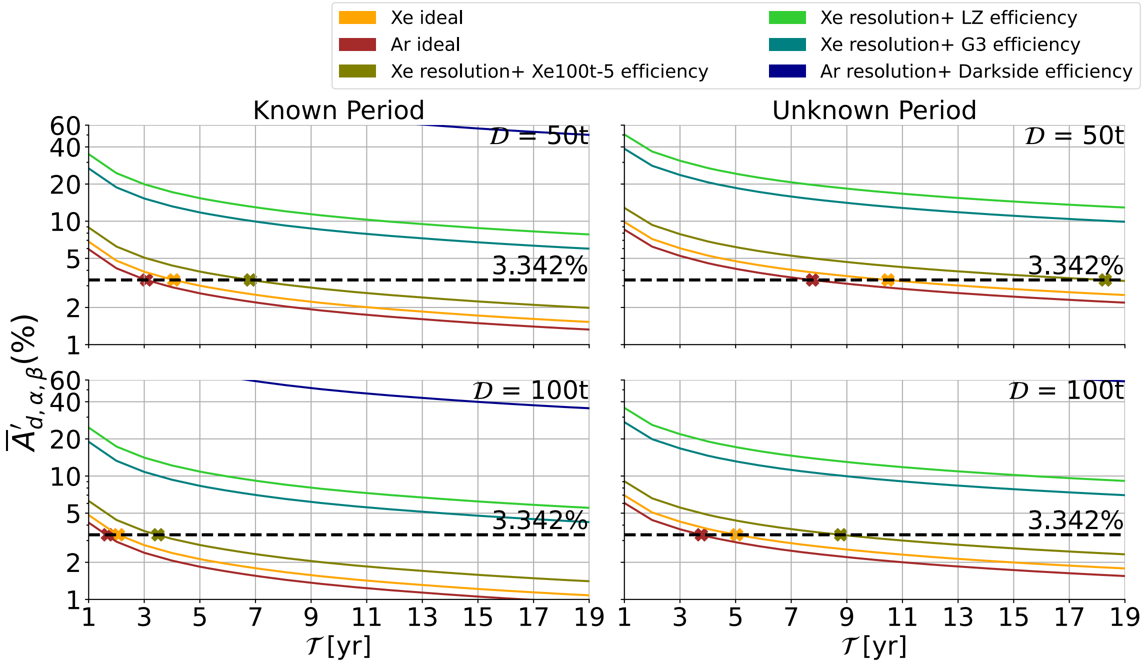

FIG. 13. The detectable amplitude for ^{8}B neutrinos through CEνNS with 90% power and 10% level of significance ($\alpha = 0.1, \beta = 0.1$), estimated from Eq. (14) as a function of detector run-time $\mathcal{T}$, for $\mathcal{D}' = 50$, 100 ton, under known period and unknown period scenarios, when $\Delta t = 10$ days. The dashed line is the amplitude of yearly modulation $A_{ecc} = 0.03342$. Crosses indicate the run-time $\mathcal{T}$ when $\bar{A}'_{d,\alpha=0.1,\beta=0.1}$ reaches A_{ecc}. Configurations of ($\mathcal{R}'_s$, $\mathcal{R}'_b$, $\mathcal{D}'$) from different detector target, resolution, and efficiency are indicated.

We see that for a $2\nu\beta\beta$ fraction $\lesssim$10% at the assumed exposure the experiment will be sensitive to the time variation from eccentricity. Also shown as the lower horizontal lines are the upper limits on the day-night modulation of the ^{7}Be component from Borexino, $A_d = A_{DN}/\sqrt{2} \approx 0.009$ [17]. This shows that a $2\nu\beta\beta$ fraction in xenon at a level ~1% has a detectable amplitude with 90% power similar to the best-fit amplitude A_d from Borexino.[4] The xenon measurements are sensitive to the lower energy pp component, for which there are no strong bounds on the time variation.

---

[4] Although these two amplitudes are similar, they cannot be compared directly since the Borexino result comes from fitting the binned data and our result comes from the likelihood ratio test.

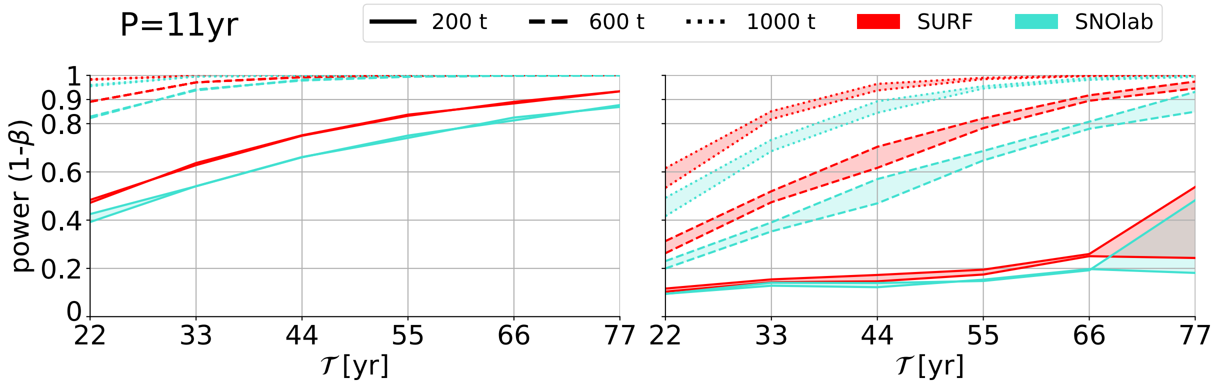

FIG. 14. Power for detecting atmospheric neutrino time variation at SURF and SNOlab through nuclear recoils under known period (left) and unknown period (right) scenarios for $\alpha = 0.1$, as a function of detector run-time $\mathcal{T}$. The assumed detector sizes $\mathcal{D}$ are 200, 600, 1000 ton. Bands indicate the differences between $\Delta t = 10$ and $\Delta t = 30$ days for assumptions of an ideal detector.

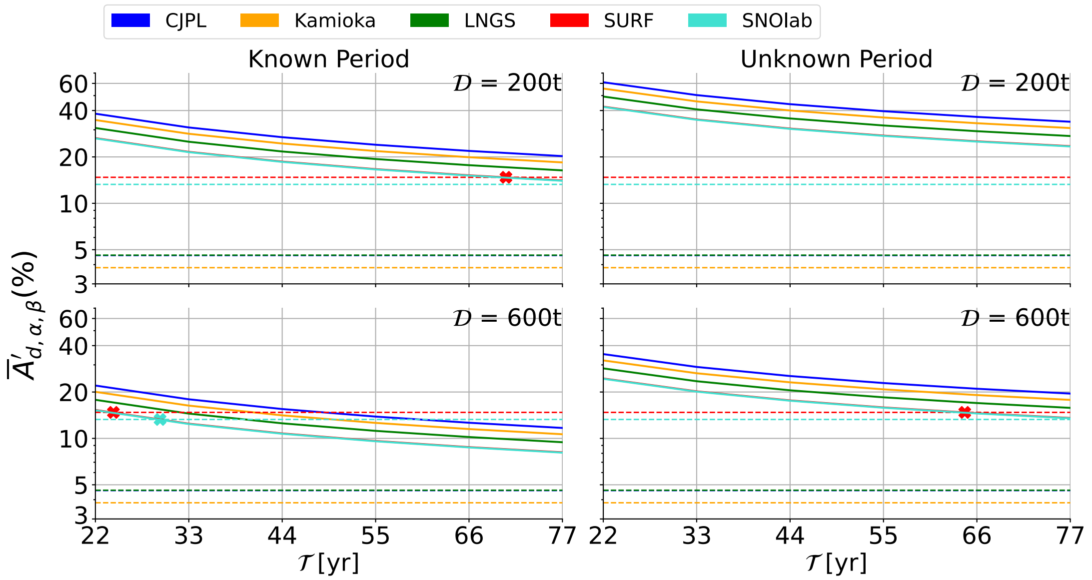

FIG. 15. The detectable amplitude for atmospheric neutrinos through CEνNS with 90% power and 10% level of significance ($\alpha = 0.1$, $\beta = 0.1$), estimated via Eq. (14) as a function of detector run-time $\mathcal{T}$, for $\mathcal{D}' = 200$, 600 ton, under known period and unknown period scenarios, when $\Delta t = 30$ days. The dashed horizontal lines are A_{atm} in Sec. III C, and each color is a different location as indicated. Crosses indicate the run-time $\mathcal{T}$ when $\bar{A}'_{d,\alpha=0.1,\beta=0.1}$ reaches A_{atm} at the corresponding location. A xenon detector with ideal resolution and efficiency is assumed.

Moving on to the CEνNS channel using the ^{8}B flux, Fig. 9 shows the required amplitude for the 90% detection at $\alpha = 0.1$, as a function of nuclear recoil energy threshold. Shown are the results for different assumptions of the efficiency, in one case showing both perfect efficiency and in the remaining cases using the detector efficiency and energy resolution modeled from NEST simulations (Fig. 3). From Fig. 9 we see that the eccentricity is clearly detectable for the assumed exposure of 100 ton and 10 yr for the ideal case. For the case with the efficiency and resolution corrections added, for thresholds $\lesssim 1$ keV there is a saturation and the eccentricity is nearly detectable given the specifications used. Note that since ^{8}B neutrinos are detected via a neutral current interaction, there is no sensitivity to the day-night effect in the CEνNS channel (there could be sensitivity if radiative corrections were detectable [47]).

Figure 10 shows the power of detecting daily and yearly time variation through electron recoils as a function of detector run-time, for an assumed 100-ton detector size. We see that even for large $2\nu\beta\beta$ fractions, the eccentricity will be detectable at 90% chance under the known period scenario with an exposure of $\lesssim 10$ yr. Here we choose a time binning of $\Delta t = 10$ days, though we find that our results are relatively insensitive to the time binning. Similarly, under the known period scenario, the Borexino sensitivity can be achieved at 90% chance for run times ∼7 yr when background includes only $2\nu\beta\beta$ and is depleted to 0.1%.

Figure 11 shows the 90% detection amplitude of detecting time variation through electron recoils as a function of detector run-time for $\Delta t = 0.05$ days and an assumed 50-ton exposure. The 3% eccentricity will be detectable with 90% power under the known period scenario within ∼13 yr for large $2\nu\beta\beta$ fractions and other backgrounds, while $2\nu\beta\beta$ needs to be depleted down to $\lesssim$0.1% to achieve the similar result under the unknown period scenario. For daily variations, a nearly fully depleted detector will be able to match the Borexino upper limits on daily time variation for a run-time of $\lesssim$13 yr under the known period scenario.

Figure 12 shows the power of detecting time variation of ^{8}B as a function of detector run-time, for an assumed detector size of 100 ton. Here we see that for an idealized detector, yearly time modulation is detectable at 90% for a run-time of ∼3 yr under the known period scenario and ∼5 yr under the unknown period scenario. We note that this is similar to the time for detection of eccentricity using the electron recoil channel, for a low $2\nu\beta\beta$ fraction. For the Xe100t-5 efficiency model, the detection timescale increases to $\lesssim$15 yr.

Figure 13 shows amplitude for 90% detection of time variation of an arbitrary amplitude for ^{8}B as a function of detector run-time for $\Delta t = 10$ days and an assumed 50- or 100-ton exposure. From this we again see that the eccentricity will be detectable with 90% power under the known period scenario within $\lesssim$10 yr for idealized detector or the resolution + Xe100t-5 efficiency detector. Under the unknown period scenario, an idealized detector is needed to achieve the similar run-time for a 50- or 100-ton detector.

We finally checked the prospects for detection of time variation of atmospheric neutrinos. The resulting power for detecting the modulation of atmospheric neutrinos from Sec. III C at each location (the amplitude A_{atm} is 0.0459 at CJPL, 0.0382 at Kamioka, 0.0461 at LNGS, 0.1475 at SURF, and 0.1327 at SNOlab) is shown in Fig. 14, for the case of an ideal detector with no efficiency or energy resolution correction. Given that the signal is weaker than the signal for solar neutrinos, in this case we consider larger detector volumes of 200, 600, and 1000 ton and plot the power as a function of the experimental run-time. Figure 15 shows the 90% amplitude of detecting time variation of atmospheric neutrinos as a function of detector run-time for $\Delta t = 30$ days and an assumed 200- or 600-ton exposure. Though the experimental volumes considered in Figs. 14 and 15 are larger than that in our solar neutrino analysis, they provide a sense of what will be required to detect the atmospheric time variation.

VII. CONCLUSIONS

In this paper, we have studied the prospects for detecting time variation of solar and atmospheric neutrinos in future large-scale xenon and argon dark matter detectors. We have developed rigorous statistical methods for detecting a time-varying signal and compared the statistical methods under the assumptions that we are searching for a known periodicity or an unknown periodicity.

For time-varying signals, we have focused on detecting solar neutrinos through ES and CEνNS. In the ES channel, for a 100-ton xenon detector running for ten years with a xenon-136 fraction of $\lesssim$0.1%, a time-variation amplitude of ∼1% is detectable for the experimental configurations that we study. This is sufficient to detect time variation due to eccentricity. For this same run-time, xenon experiments will achieve similar sensitivity to the Borexino experiment for daily modulations that will be induced from the propagation of electron neutrinos through Earth. Both of these results will hold if the $2\nu\beta\beta$ fraction can be reduced to $\lesssim$0.01.

In the CEνNS channel, we find that for a threshold of 1 keV, a detector with ideal efficiency and energy resolution will be sensitive to a yearly variation in the flux. For a detector with efficiency and resolution similar to current xenon experiments, detectors will approach sensitivity to the eccentricity for thresholds $\lesssim$1 keV. In comparison to previous studies that considered the time variation in the nuclear recoil channel due to the eccentricity [10], we add the more realistic detector scenarios to our modeling. The detector modeling effects most strongly affect the CEνNS channel, whereas the ES channel is most strongly affected by the $2\nu\beta\beta$ fraction, as discussed above.

Dark matter experiments provide the unique possibility to measure the time variation of the solar neutrino flux through multiple detection channels. Detecting eccentricity in both channels would be important because it confirms the solar origin of the signal. Further, it provides a test for the long term stability of the detector and provides a means to identify possible time-varying signals of unknown origin.

ACKNOWLEDGMENTS

Y. Z. and L. E. S. are supported by the DOE Grant No. DE-SC0010813.

APPENDIX: CRITICAL VALUES FOR DIFFERENT VALUES OF Δt AND $\mathcal{T}$

Table VII shows the critical values $LS_{\max,\alpha,1}$ and $LS_{\max,\alpha,2}$ for $\Delta t = 0.2$ days and $\mathcal{T}$ from 1 to 20 yr.

Table VIII shows the critical values $LS_{\max,\alpha,1}$ and $LS_{\max,\alpha,2}$ for $\Delta t = 5$ days and $\mathcal{T}$ from 1 to 22 yr.

Table IX shows the critical values $LS_{\max,\alpha,1}$ and $LS_{\max,\alpha,2}$ for $\Delta t = 10$ days and $\mathcal{T}$ from 1 to 22 yr.

TABLE VII. Critical values for $\Delta t = 0.2$ days, $f_{\text{scan}} = [1/365.25\ \text{day}^{-1}, 1\ \text{day}^{-1}]$, $n_o = 10$, $f_{\text{adj}} = 1.5$.

			$\alpha = 0.1$		$\alpha = 0.05$		$\alpha = 0.02$	
$\mathcal{T}$ (yr)	$\mathcal{M}_{\text{entire}}$	$\mathcal{M}_{\text{scan}}$	$LS_{\max,\alpha,1}$	$LS_{\max,\alpha,2}$	$LS_{\max,\alpha,1}$	$LS_{\max,\alpha,2}$	$LS_{\max,\alpha,1}$	$LS_{\max,\alpha,2}$
1	12175	2429	10.05	9.83	10.77	10.56	11.7	11.37
2	24350	4859	10.74	10.42	11.46	11.25	12.39	12.27
3	36525	7288	11.14	10.98	11.86	11.71	12.8	12.87
4	48700	9718	11.43	11.18	12.15	11.89	13.08	12.68
5	60875	12148	11.66	11.39	12.38	12.15	13.31	13.07
6	73050	14577	11.84	11.73	12.56	12.47	13.49	13.28
7	85225	17007	11.99	12.05	12.71	12.84	13.64	13.84
8	97400	19437	12.13	11.89	12.85	12.7	13.78	13.79
9	109575	21866	12.24	12.01	12.96	12.76	13.89	13.58
10	121750	24296	12.35	12.14	13.07	12.87	14.0	13.83
11	133925	26726	12.44	12.34	13.16	13.11	14.1	14.0
12	146100	29155	12.53	12.49	13.25	13.24	14.18	14.33
13	158275	31585	12.61	12.62	13.33	13.32	14.26	14.24
14	170450	34015	12.68	12.78	13.4	13.53	14.34	14.46
15	182625	36444	12.75	12.54	13.47	13.23	14.41	14.2
16	194800	38874	12.82	12.61	13.54	13.33	14.47	14.21
17	206975	41304	12.88	12.66	13.6	13.37	14.53	14.22
18	219150	43733	12.94	12.77	13.66	13.51	14.59	14.3
19	231325	46163	12.99	12.75	13.71	13.45	14.64	14.53
20	243500	48593	13.04	12.97	13.76	13.69	14.69	14.65

TABLE VIII. Critical values for $\Delta t = 5$ days, $f_{\text{scan}} = [1/365.25\ \text{day}^{-1}, 1/5\ \text{day}^{-1}]$, $n_o = 10$.

				$\alpha = 0.1$		$\alpha = 0.05$		$\alpha = 0.02$	
f_{adj}	$\mathcal{T}$ (yr)	$\mathcal{M}_{\text{entire}}$	$\mathcal{M}_{\text{scan}}$	$LS_{\max,\alpha,1}$	$LS_{\max,\alpha,2}$	$LS_{\max,\alpha,1}$	$LS_{\max,\alpha,2}$	$LS_{\max,\alpha,1}$	$LS_{\max,\alpha,2}$
7	1	104	104	6.9	6.79	7.61	7.44	8.55	8.39
6	2	243	243	7.74	7.68	8.46	8.43	9.4	9.53
6	3	365	365	8.15	8.66	8.87	9.92	9.8	12.29
6	4	487	487	8.44	8.55	9.16	9.32	10.09	10.66
6	5	608	608	8.66	8.44	9.38	9.14	10.31	9.96
6	6	730	730	8.84	9.31	9.56	10.56	10.49	12.83
6	7	852	852	9.0	8.96	9.72	9.67	10.65	10.62
6	8	974	974	9.13	9.14	9.85	9.94	10.78	10.92
6	9	1095	1095	9.25	9.14	9.97	9.85	10.9	10.84
6	10	1217	1217	9.35	9.23	10.07	9.98	11.01	11.03
6	11	1339	1339	9.45	9.48	10.17	10.3	11.1	11.34
6	12	1461	1461	9.54	10.0	10.26	11.05	11.19	13.2
6	13	1582	1582	9.62	9.58	10.34	10.4	11.27	11.26
6	14	1704	1704	9.69	9.71	10.41	10.52	11.34	11.64
6	15	1826	1826	9.76	9.83	10.48	10.59	11.41	11.56
6	16	1948	1948	9.82	9.94	10.54	10.68	11.48	11.63
6	17	2069	2069	9.89	10.12	10.61	10.9	11.54	11.98
6	18	2191	2191	9.94	9.8	10.66	10.59	11.59	11.51
6	19	2313	2313	10.0	9.91	10.72	10.63	11.65	11.57
6	20	2435	2435	10.05	10.03	10.77	10.77	11.7	11.68
6	21	2556	2556	10.1	10.16	10.82	10.87	11.75	12.0
6	22	2678	2678	10.14	10.12	10.86	10.83	11.79	11.9

TABLE IX. Critical values for $\Delta t = 10$ days, $f_{\mathrm{scan}} = [1/365.25\ \mathrm{day}^{-1},\ 1/10\ \mathrm{day}^{-1}]$, $n_o = 10$.

				$\alpha = 0.1$		$\alpha = 0.05$		$\alpha = 0.02$	
f_{adj}	$\mathcal{T}$ (yr)	$\mathcal{M}_{\mathrm{entire}}$	$\mathcal{M}_{\mathrm{scan}}$	$LS_{\max,\alpha,1}$	$LS_{\max,\alpha,2}$	$LS_{\max,\alpha,1}$	$LS_{\max,\alpha,2}$	$LS_{\max,\alpha,1}$	$LS_{\max,\alpha,2}$
7	1	52	52	6.2	5.76	6.92	6.42	7.85	7.28
7	2	104	104	6.9	6.88	7.61	7.62	8.55	8.63
6	3	182	182	7.45	8.47	8.17	10.26	9.11	13.55
6	4	243	243	7.74	7.57	8.46	8.35	9.4	9.42
6	5	304	304	7.97	7.66	8.69	8.32	9.62	9.35
6	6	365	365	8.15	9.07	8.87	10.64	9.8	14.11
6	7	426	426	8.3	8.1	9.02	8.83	9.96	9.66
6	8	487	487	8.44	8.42	9.16	9.21	10.09	10.35
6	9	547	547	8.55	8.35	9.27	9.03	10.21	9.91
6	10	608	608	8.66	8.4	9.38	9.2	10.31	10.11
6	11	669	669	8.76	8.68	9.48	9.45	10.41	10.61
6	12	730	730	8.84	9.92	9.56	12.1	10.49	16.08
6	13	791	791	8.92	8.86	9.64	9.55	10.58	10.43
6	14	852	852	9.0	8.86	9.72	9.55	10.65	10.64
6	15	913	913	9.07	8.96	9.79	9.67	10.72	10.69
6	16	974	974	9.13	9.23	9.85	10.06	10.78	11.24
6	17	1034	1034	9.19	9.38	9.91	10.21	10.84	11.11
6	18	1095	1095	9.25	9.12	9.97	9.88	10.9	10.79
6	19	1156	1156	9.3	9.2	10.02	10.0	10.95	10.89
6	20	1217	1217	9.35	9.33	10.07	10.03	11.01	11.04
6	21	1278	1278	9.4	9.28	10.12	10.04	11.05	11.07
6	22	1339	1339	9.45	9.45	10.17	10.23	11.1	11.23

[1] E. Aprile *et al.* (XENON Collaboration), Phys. Rev. Lett. **121**, 111302 (2018).

[2] J. Aalbers *et al.* (LUX-ZEPLIN Collaboration), Phys. Rev. Lett. **131**, 041002 (2023).

[3] J. Aalbers *et al.*, J. Phys. G **50**, 013001 (2023).

[4] J. Billard, L. Strigari, and E. Figueroa-Feliciano, Phys. Rev. D **89**, 023524 (2014).

[5] B. Dutta and L. E. Strigari, Annu. Rev. Nucl. Part. Sci. **69**, 137 (2019).

[6] J. B. Dent, B. Dutta, J. L. Newstead, and L. E. Strigari, Phys. Rev. D **93**, 075018 (2016).

[7] J. B. Dent, B. Dutta, J. L. Newstead, and L. E. Strigari, Phys. Rev. D **95**, 051701 (2017).

[8] G. Herrera, J. High Energy Phys. 05 (2024) 288.

[9] C. A. J. O'Hare, A. M. Green, J. Billard, E. Figueroa-Feliciano, and L. E. Strigari, Phys. Rev. D **92**, 063518 (2015).

[10] J. H. Davis, J. Cosmol. Astropart. Phys. 03 (2015) 012.

[11] S. Sassi, A. Dinmohammadi, M. Heikinheimo, N. Mirabolfathi, K. Nordlund, H. Safari, and K. Tuominen, Phys. Rev. D **104**, 063037 (2021).

[12] D. G. Cerdeño, M. Fairbairn, T. Jubb, P. A. N. Machado, A. C. Vincent, and C. Bœhm, J. High Energy Phys. 05 (2016) 118; 09 (2016) 048.

[13] D. Aristizabal Sierra, B. Dutta, S. Liao, and L. E. Strigari, J. High Energy Phys. 12 (2019) 124.

[14] D. Aristizabal Sierra, V. De Romeri, L. J. Flores, and D. K. Papoulias, J. Cosmol. Astropart. Phys. 01 (2022) 055.

[15] Y. Zhuang, L. E. Strigari, and R. F. Lang, Phys. Rev. D **105**, 043001 (2022).

[16] C. A. J. O'Hare, Phys. Rev. Lett. **127**, 251802 (2021).

[17] S. Appel *et al.* (Borexino Collaboration), Astropart. Phys. **145**, 102778 (2023).

[18] G. Ranucci, Phys. Rev. D **73**, 103003 (2006).

[19] K. Abe *et al.* (Super-Kamiokande Collaboration), Phys. Rev. D **94**, 052010 (2016).

[20] Y. Zhuang, L. E. Strigari, L. Jin, and S. Sinha, Phys. Rev. D **109**, 043055 (2024).

[21] W. C. Haxton, R. G. Hamish Robertson, and A. M. Serenelli, Annu. Rev. Astron. Astrophys. **51**, 21 (2013).

[22] J. L. Newstead, L. E. Strigari, and R. F. Lang, Phys. Rev. D **99**, 043006 (2019).

[23] D. Franco *et al.*, J. Cosmol. Astropart. Phys. 08 (2016) 017.

[24] A. M. Suliga, J. F. Beacom, and I. Tamborra, Phys. Rev. D **105**, 043008 (2022).

[25] M. Szydagis, N. Barry, K. Kazkaz, J. Mock, D. Stolp, M. Sweany, M. Tripathi, S. Uvarov, N. Walsh, and M. Woods, J. Instrum. **6**, P10002 (2011).

[26] J. L. Newstead, R. F. Lang, and L. E. Strigari, Phys. Rev. D **104**, 115022 (2021).

[27] E. Aprile *et al.* (XENON Collaboration), Phys. Rev. D **102**, 072004 (2020).

[28] P. Agnes, L. Agostino, I. F. M. Albuquerque, T. Alexander, A. K. Alton, K. Arisaka, H. O. Back, B. Baldin, K. Biery, G. Bonfini *et al.*, Phys. Rev. D **93**, 081101 (2016).

[29] Borexino Collaboration, G. Bellini, J. Benziger, D. Bick, G. Bonfini, D. Bravo, M. B. Avanzini, B. Caccianiga, L. Cadonati, F. Calaprice *et al.*, Phys. Rev. D **89**, 112007 (2014).

[30] M. J. Lewis and K. Freese, Phys. Rev. D **70**, 043501 (2004).

[31] P. Sturrock, G. Walther, and S. Wheatland, Astrophys. J. **491**, 409 (2009).

[32] L. Pandola, Astropart. Phys. **22**, 219 (2004).

[33] B. Aharmim, S. N. Ahmed, A. E. Anthony, E. W. Beier, A. Bellerive, M. Bergevin, S. D. Biller, M. G. Boulay, M. G. Bowler, Y. D. Chan *et al.*, Phys. Rev. D **72**, 052010 (2005).

[34] G. Ranucci and M. Rovere, Phys. Rev. D **75**, 013010 (2007).

[35] G. Bellini *et al.* (Borexino Collaboration), Phys. Lett. B **707**, 22 (2012).

[36] M. Agostini, K. Altenmüller, S. Appel, V. Atroshchenko, D. Basilico, G. Bellini, J. Benziger, D. Bick, G. Bonfini, L. Borodikhina *et al.*, Astropart. Phys. **92**, 21 (2017).

[37] J. Yoo, Y. Ashie, S. Fukuda, Y. Fukuda, K. Ishihara, Y. Itow, Y. Koshio, A. Minamino, M. Miura, S. Moriyama *et al.*, Phys. Rev. D **68**, 092002 (2003).

[38] P. A. Sturrock, Astrophys. J. **594**, 1102 (2003).

[39] P. A. Sturrock, D. O. Caldwell, J. D. Scargle, and M. S. Wheatland, Phys. Rev. D **72**, 113004 (2005).

[40] J. Hosaka, K. Ishihara, J. Kameda, Y. Koshio, A. Minamino, C. Mitsuda, M. Miura, S. Moriyama, M. Nakahata, T. Namba *et al.*, Phys. Rev. D **73**, 112001 (2006).

[41] K. Abe, C. Bronner, Y. Hayato, K. Hiraide, K. Hosokawa, K. Ieki, M. Ikeda, J. Kameda, Y. Kanemura, R. Kaneshima *et al.*, Phys. Rev. Lett. **132**, 241803 (2024).

[42] P. Heix, S. Tilav, C. Wiebusch, and M. Zöcklein, *Proc. Sci.*, ICRC2019 (2020) 465 [arXiv:1909.02036].

[43] J. D. Scargle, Astrophys. J. **263**, 835 (1982).

[44] J. T. VanderPlas, Astrophys. J. Suppl. Ser. **236**, 16 (2018).

[45] P. Virtanen, R. Gommers, T. E. Oliphant, M. Haberland, T. Reddy, D. Cournapeau, E. Burovski, P. Peterson, W. Weckesser, J. Bright *et al.*, Nat. Methods **17**, 261 (2020).

[46] A. M. Price-Whelan, B. Sipőcz, H. Günther, P. Lim, S. Crawford, S. Conseil, D. Shupe, M. Craig, N. Dencheva, A. Ginsburg *et al.*, Astron. J. **156**, 123 (2018).

[47] N. Mishra and L. E. Strigari, Phys. Rev. D **108**, 063023 (2023).